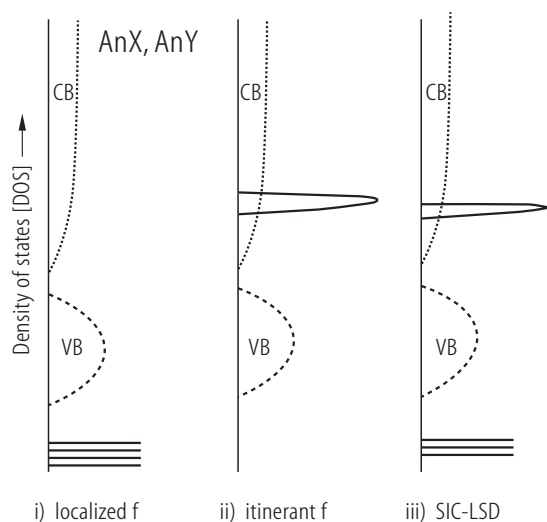
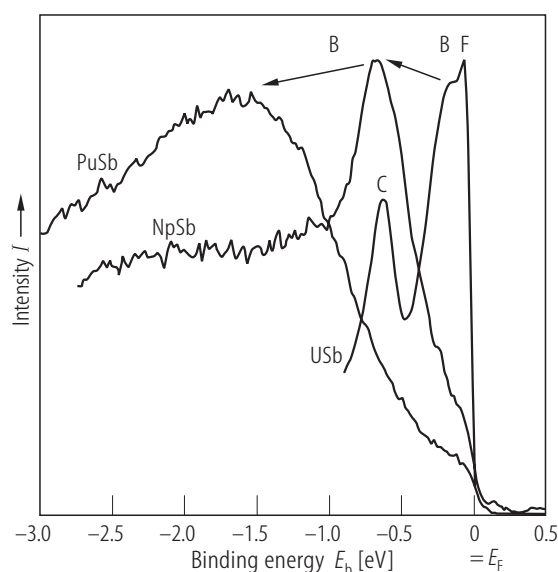


## 1.3.1.1.4 Figures and tables

## R. AnX. General properties of actinide monpnictides



**Fig. R.1A.** AnX, AnY. *Ab initio* band structure treatments. Schematic representation of the density of states (DOS) for the actinide monpnictides AnX (or monochalcogenides AnY). Local spin density (LSD) approach - all electrons are treated as inert core electrons, ii) LSD - approach treating f-electrons as band states and iii) SIC (self interaction corrected) - LSD approach with both localized and delocalized f states. The dashed lines represent the ligand p-band, treated as a predominate contribution of valence band (VB). This picture has been adopted for generalizing the band structure approaches for all actinide monpnictides, while originally it was used to represent the situation in the Pu-monpnictides [02PSTS]. If for both former cases i) and ii) the f-electron degrees of freedom are available for the formation of band states, the latter approach iii) allows for an integer number of f-states to be localized. For example, in the case of Pu-monocompounds the SIC - LSD approach allows to interpret the experimental data in terms of the coexistence of both localized and delocalized f-states.



**Fig. R.1B.** AnSb s.c. The comparisons of angle-integrated PES results for three monpnictides AnSb (An=U, Np, Pu) [04DJLB]. Note that for the compounds there are seen the following PE peaks: one (denoted as B) for NpSb and PuSb, and as many as three (denoted F, B and C) peaks for USb with well defined 5f character within the first 3 eV of each spectrum. The peak B (broad), existing in each case, bears the majority of the spectral 5f weight, the full width at half maximum (FWHM) of which becomes smaller with diminishing binding energy.

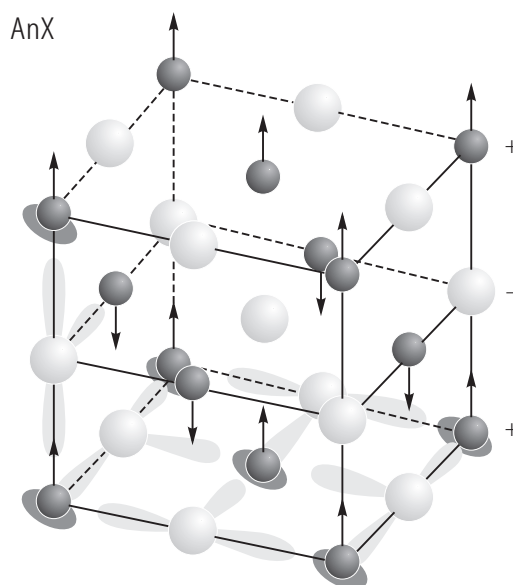


**Fig. R.2.** AnX. NaCl-type of crystal structure and magnetic interaction. The type I antiferromagnetic structure (AF I) together with schematic bonding arrangements [81SLSV]. The 5f electrons around the uranium atoms are *oblate* orbitals (solid points) interacting strongly with the anion p wave functions in the (001) plane, but considerably weaker with those above and below. The *oblate* shape of the 5f wave function has been derived from the magnetic form factor analysis [76L]. This anisotropy may relate microscopically to the covalent bonding existing between the 5f orbitals on An atoms and p orbitals on pnictogen atoms in the (001) sheets.

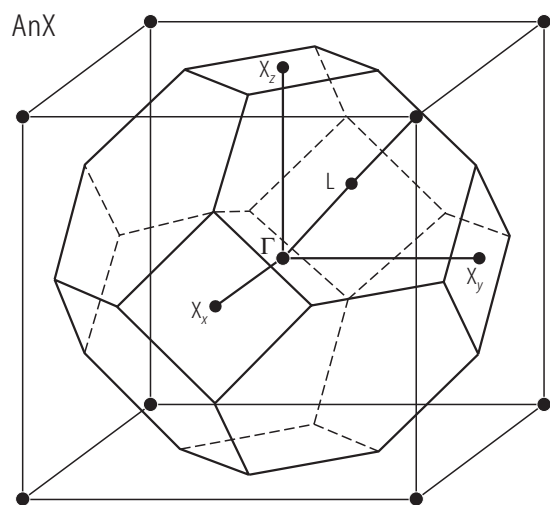


**Fig. R.3.** AnX. Full nuclear fcc Brillouin zone (BZ) independent of the realized magnetic structure taken from [86HF]. In the case of realization of magnetic structures with tetragonal symmetry (e.g. multi- $k$  configurations – see Fig. R.14) with the [001], [110] and [111] directions then the symmetry points  $X$  become different and are labeled as:  $X_x = (2\pi/a)(100)$ ,  $X_y = (2\pi/a)(010)$  and  $X_z = (2\pi/a)(001)$ .

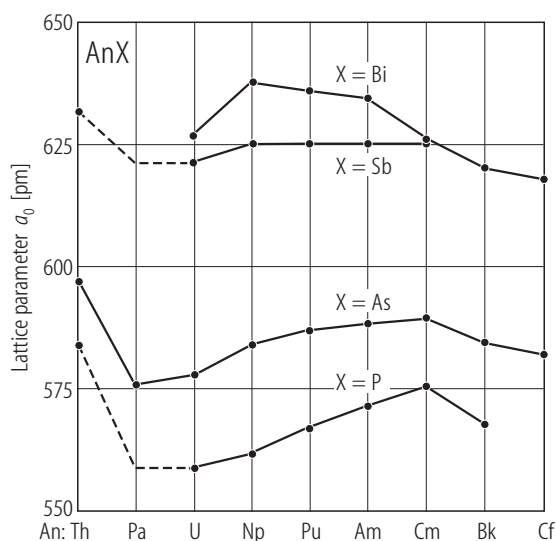
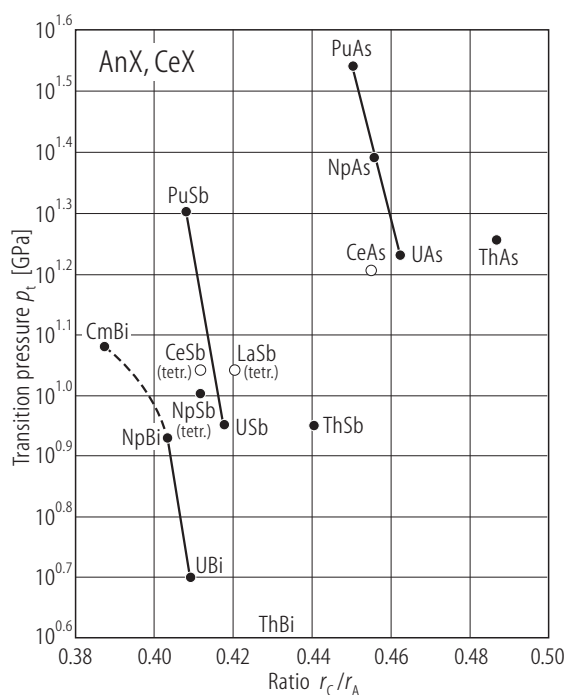


**Fig. R.4.** AnX ( $X = P, As, Sb, Bi$ ). Lattice parameters,  $a_0$ , of the actinide monopnictides [87B] (see Table 1). All of the actinide monopnictides except for ThBi are isomorphous and crystallize in the NaCl (B1)-type crystal structure. ThBi has the CsCl (B2)-type structure with the lattice parameter  $a_0 = 0.3909$  nm. As in the case of the actinide metals the deviation of the lattice parameters from a simple linear behaviour observed for the corresponding lanthanide compounds can be taken as an indication of participation of the 5f electrons in its chemical bond. The effect of bond shortening is especially seen for the monocompounds with the lighter non-actinide elements (e.g. compare Fig. I.4), i.e. for monocarbides and mononitrides. Thus the isomorphism of this large group of compounds causes that the bond length variation is reflected by the change in the lattice parameters.



For Fig. R.5 see next page

**Fig. R.6.** AnX. A semi-log plot of the transition pressure  $p_t$  for the B1 to B2 transition as a function of the cation/anion size ratio,  $r_C/r_A$ , [93B2]. Trivalent ionic radii were used for all cations. For comparison the transitions to other structures are also presented. None from the mononitrides has been observed to show a transformation to the B2-type structure under pressure. Note that except for ThAs and ThSb the transition pressure  $p_t$  increases with decreasing  $r_C/r_A$ . This indicates that the anions are more compressible than the cations. Thus, geometrical factors are considered as one of the major reasons for inducing phase transition in the actinide monopnictides, AnX.

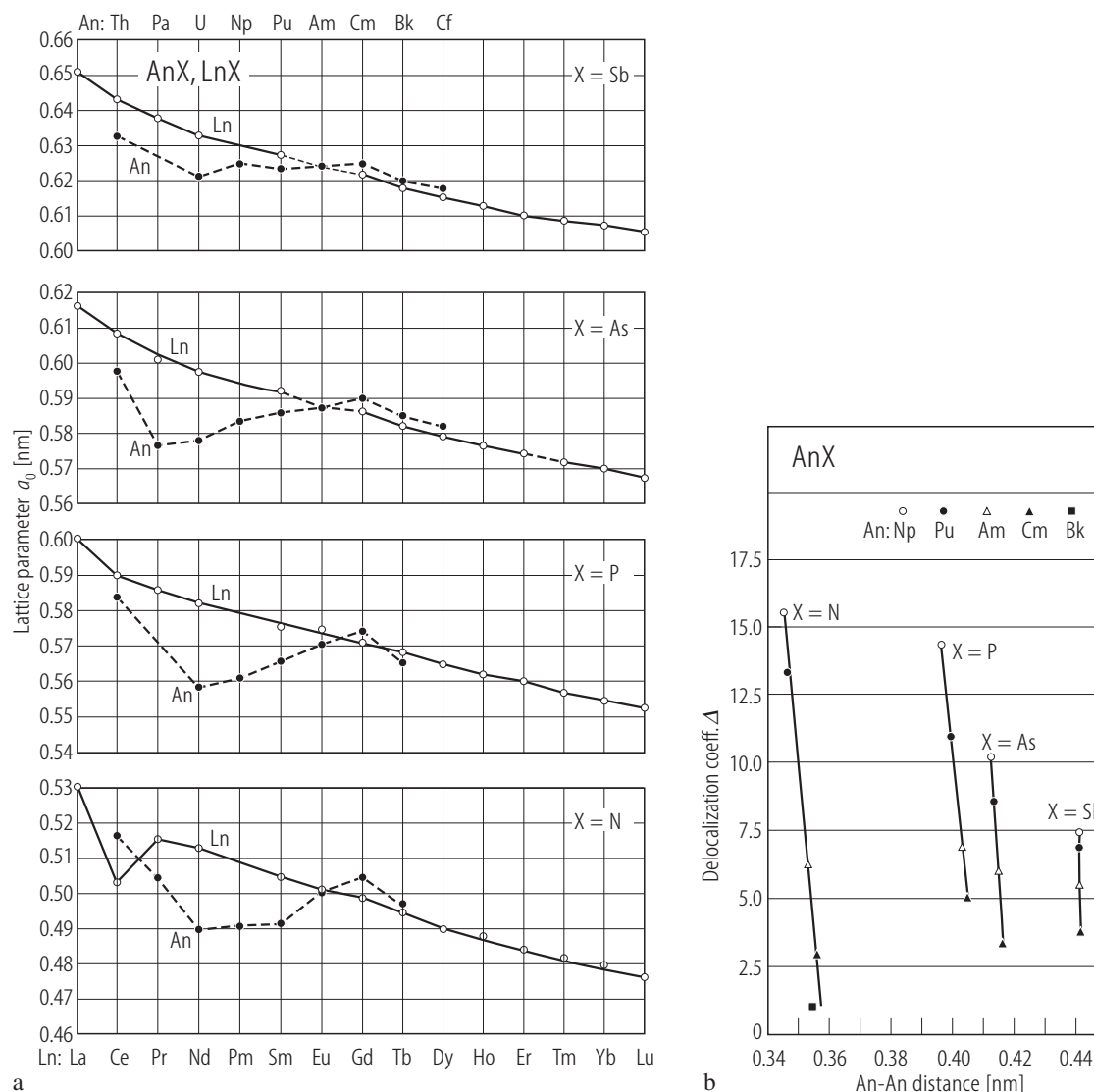


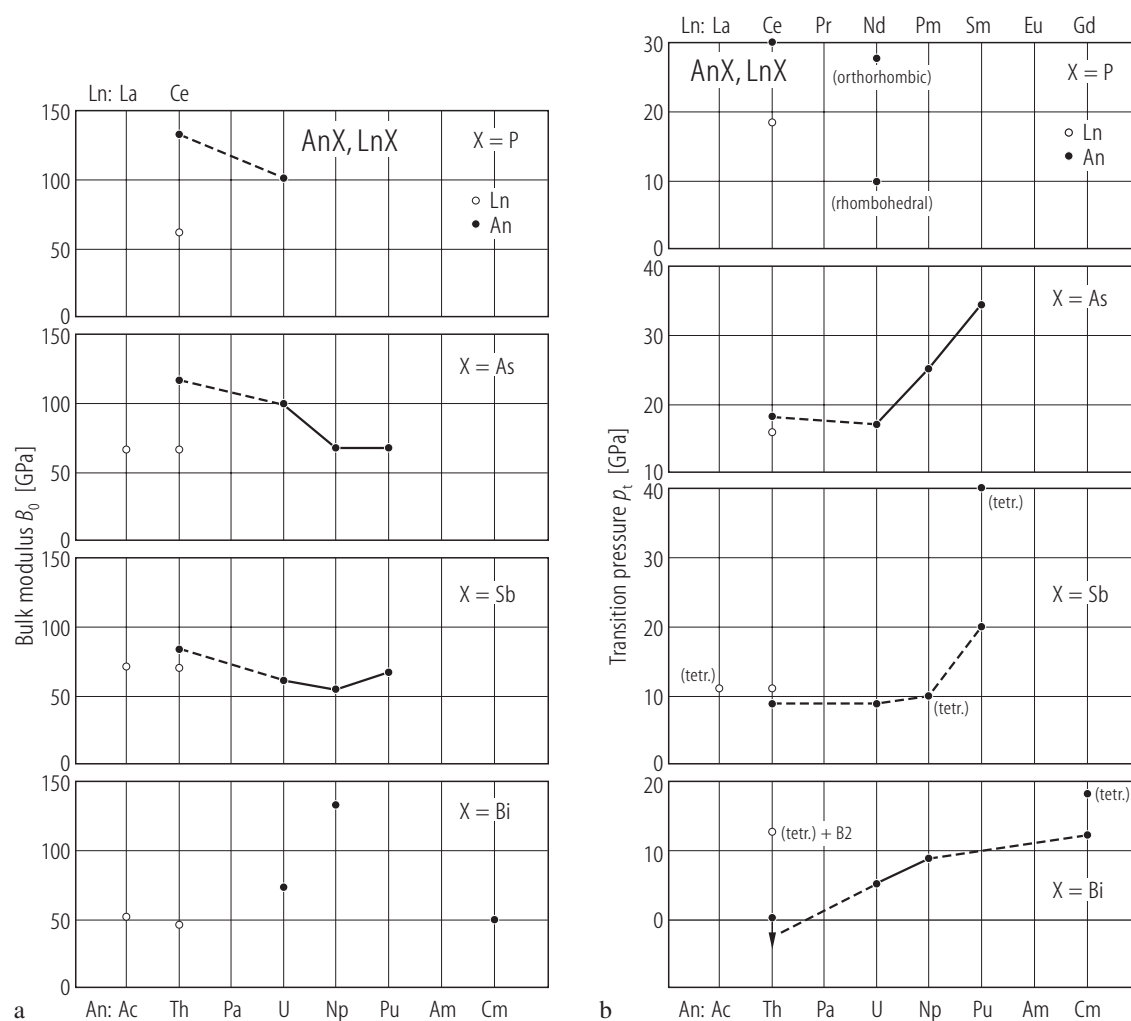
**Fig. R.5.**  $\text{AnX}$  ( $X = \text{N}, \text{P}, \text{As}, \text{Sb}$ ). ( $\text{An} = \text{Th} \dots \text{Cf}$ ). **(a)** Lattice parameters of actinide monpnictides compared to the corresponding lanthanide monpnictides [86DDT]. The main characteristics of lighter actinide monpnictides is the irregular dependence of  $a_0$  on the atomic number, with a distinct minimum around uranium. However the dip of this minimum decreases with increasing the atomic number of the coordinated ligand X. Note that the regular lattice contraction behaviour of lanthanide  $\text{LnX}$  monocompounds are achieved by actinide analogs not earlier than by the americium monpnictides,  $\text{AmX}$ . **(b)** The pheno-

menological magnitude of the 5f electron delocalization,  $\Delta$ , represented by expression:

$\Delta = 100 (V_{\text{AnX}}(\text{calc}) - V_{\text{AnX}}(\text{obs})) / V_{\text{AnX}}(\text{calc})$ ;  $V_{\text{AnX}}(\text{calc})$  has been found by comparison of two molar volume ratios:

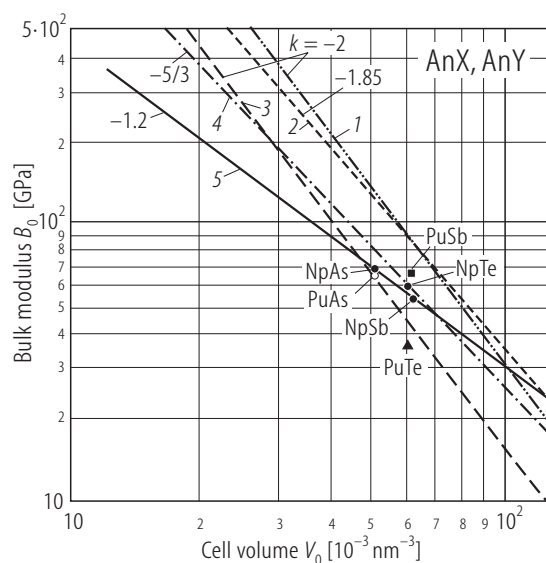
$$\frac{V_{\text{AnF}_3} - V_{\text{LnF}_3}}{V_{\text{LnF}_3}} = \frac{V_{\text{AnX}}(\text{calc}) - V_{\text{LnX}}}{V_{\text{LnX}}}. \text{ Note the decrease}$$

in  $\Delta$  with increasing Z number of an actinide ion in the monocompounds, which shows that the 5f electrons are becoming more localized. Taken from [81DD].

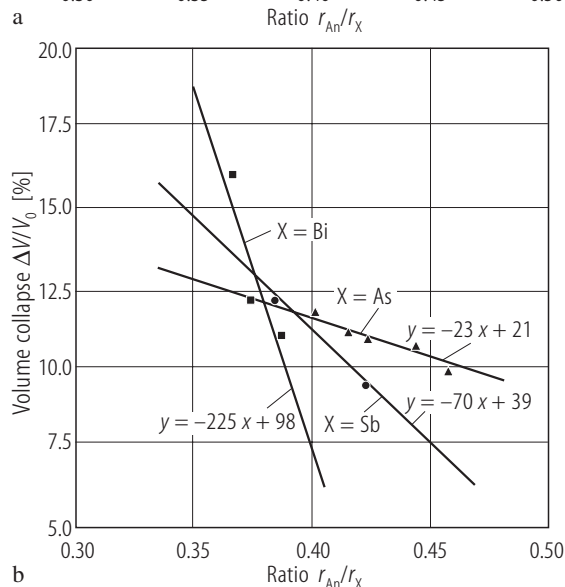
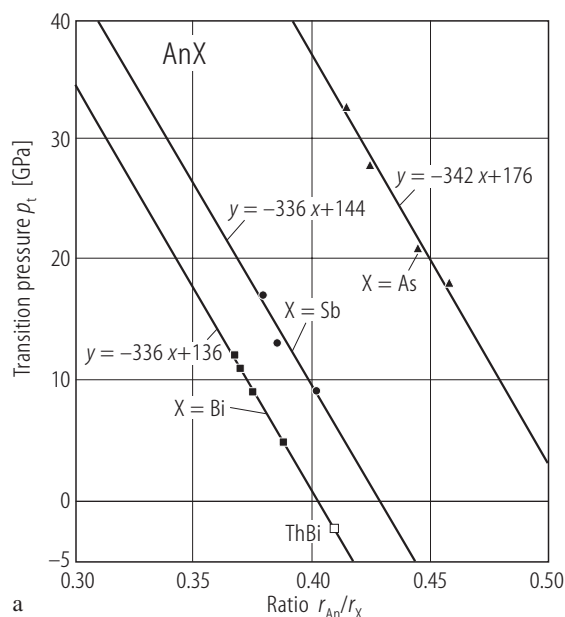


**Fig. R.7.** AnX, LnX. **(a)** Bulk moduli,  $B_0$ , determined for AnX ( $X = P, As, Sb, Bi$ ) compared to those of corresponding LnX ( $Ln = La$  and  $Ce$ ) compounds [93BH], [95B]. The general trend for AnX is a decrease of  $B_0$ -values with increasing the atomic number  $Z$  of the actinide (for  $B_0$  and pressure derivatives  $B_0'$  see Table 6). In contrast, LnX

series show practically no variation in  $B_0$  vs.  $Z$  of the lanthanide and do not exceed 70 GPa. **(b)** The transition pressures,  $p_t$  of AnX monopnictides, except for AnC and AnN, compared to those in the LnX monocompounds [93BH]. These transitions are from B1 to B2 or other structure if it is marked.



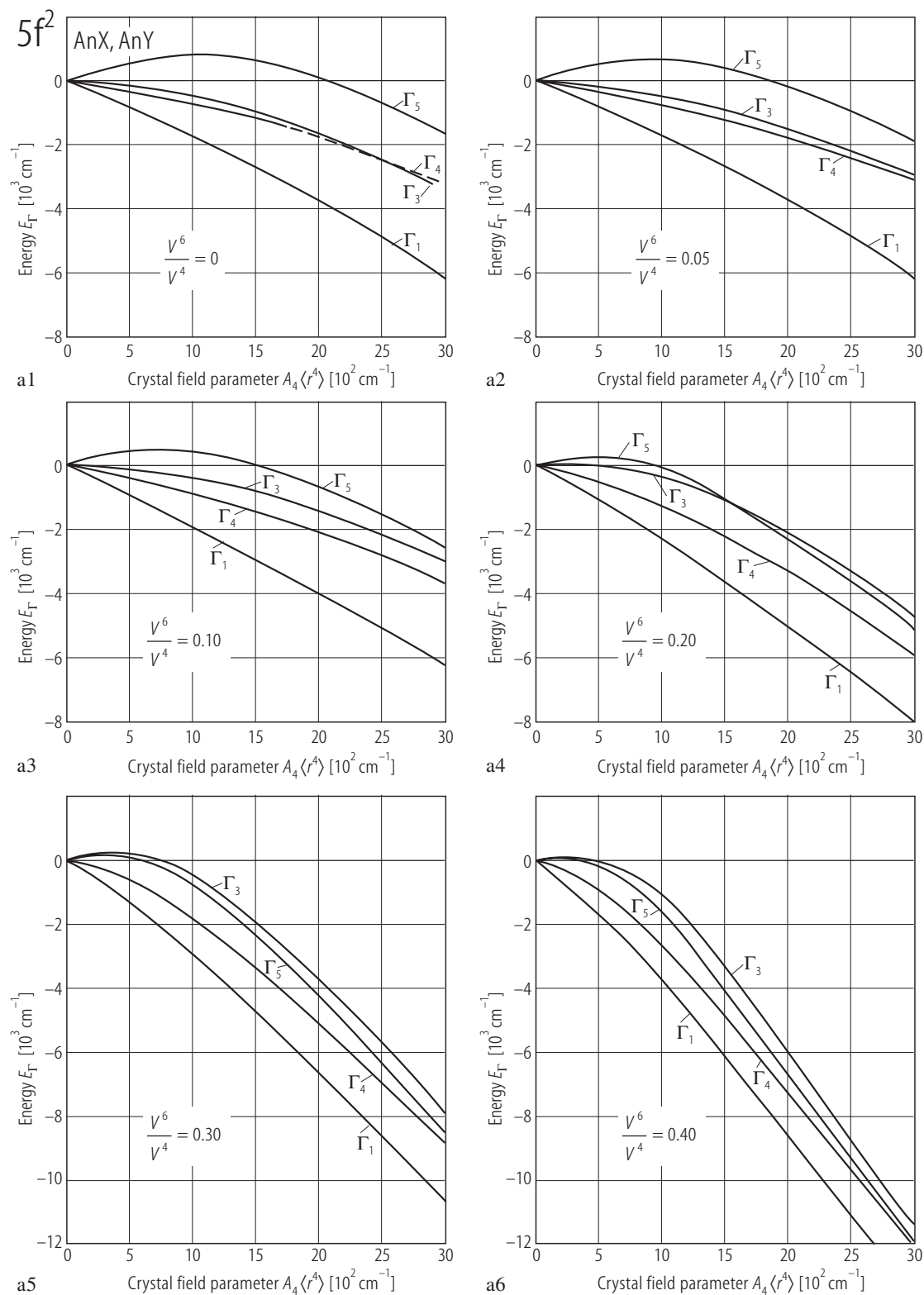
**Fig. R.8.** AnX, AnY. A log-log plot of bulk modulus,  $B_0$ , vs. cell volume per formula unit,  $V_0$ , according to the Anderson and Nafe equation:  $\ln B_0 = -k \ln V_0 + \text{constant}$  [90DBHS]. 1 – thorium monopnictides [88GSBD], 2 – thorium monochalcogenides [88SGBL], 3 – uranium monopnictides [89GSBD], 4 – uranium monochalcogenides [89GSBD], 5 – neptunium monopnictides: NpAs [86DDBS] and NpSb [90DBHS], • – NpTe [90DBHS], ○ – PuAs [89DBSP], ■ – PuSb [90DBHS], ▲ – PuTe [90DBHS]. Note that when going from Th to Np and Pu isostructural monocompounds the slope of connecting line tends to decrease to unity indicating an increasing ionic character of An-X and An-Y bondings. For PuTe, the small bulk modulus does not fit with any of the series.



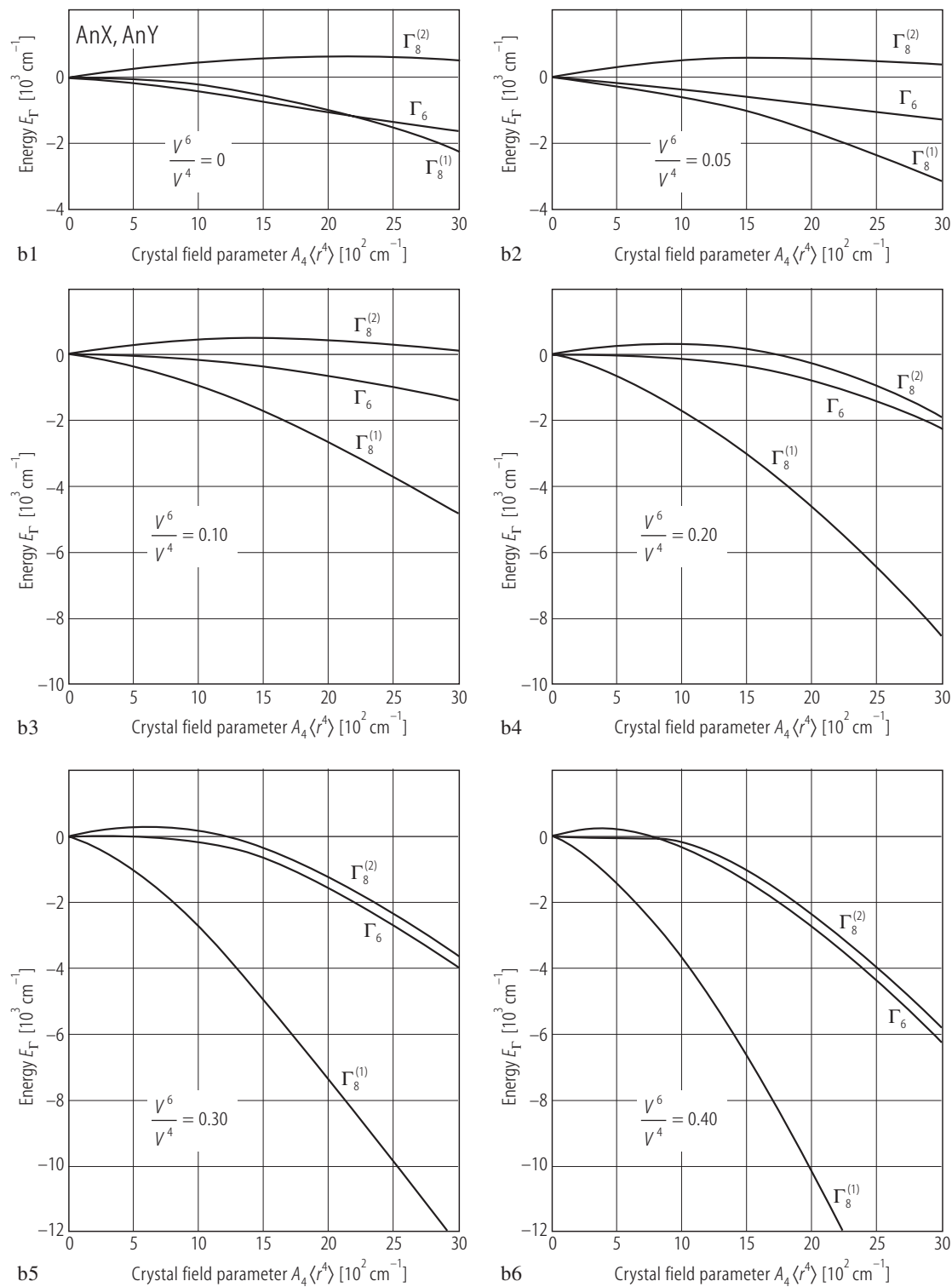
**Fig. R.9.** AnX (X = As, Sb, Bi). **(a)** The transition pressure,  $p_t$ , vs. the ratio of the ionic radii,  $r_{\text{An}}/r_X$ , in the actinide monopnictides [94G]. All three groups of monopnictides form straight lines  $y = Ax + B$ , where  $x = r_{\text{An}}/r_X$  and  $r_X = a_0/2 - r_{\text{An}}^{4+}$ . A general equation for all these monopnictides may be formulated with  $A = -339$  and  $B = 174, 145$  and  $136$  for an anion of the fourth, fifth and sixth periods, respectively including also the monochalcogenides AnSe and AnTe. **(b)** The volume collapse  $\Delta V/V_0$  (%) at the transition pressures  $p_t$  vs. the ionic radii  $r_{\text{An}}/r_X$  in the actinide monopnictides series [94G]. The relationship is presented as straight lines  $y = Cx + D$ . Note that the larger the anion the more negative is the slope  $C$ .

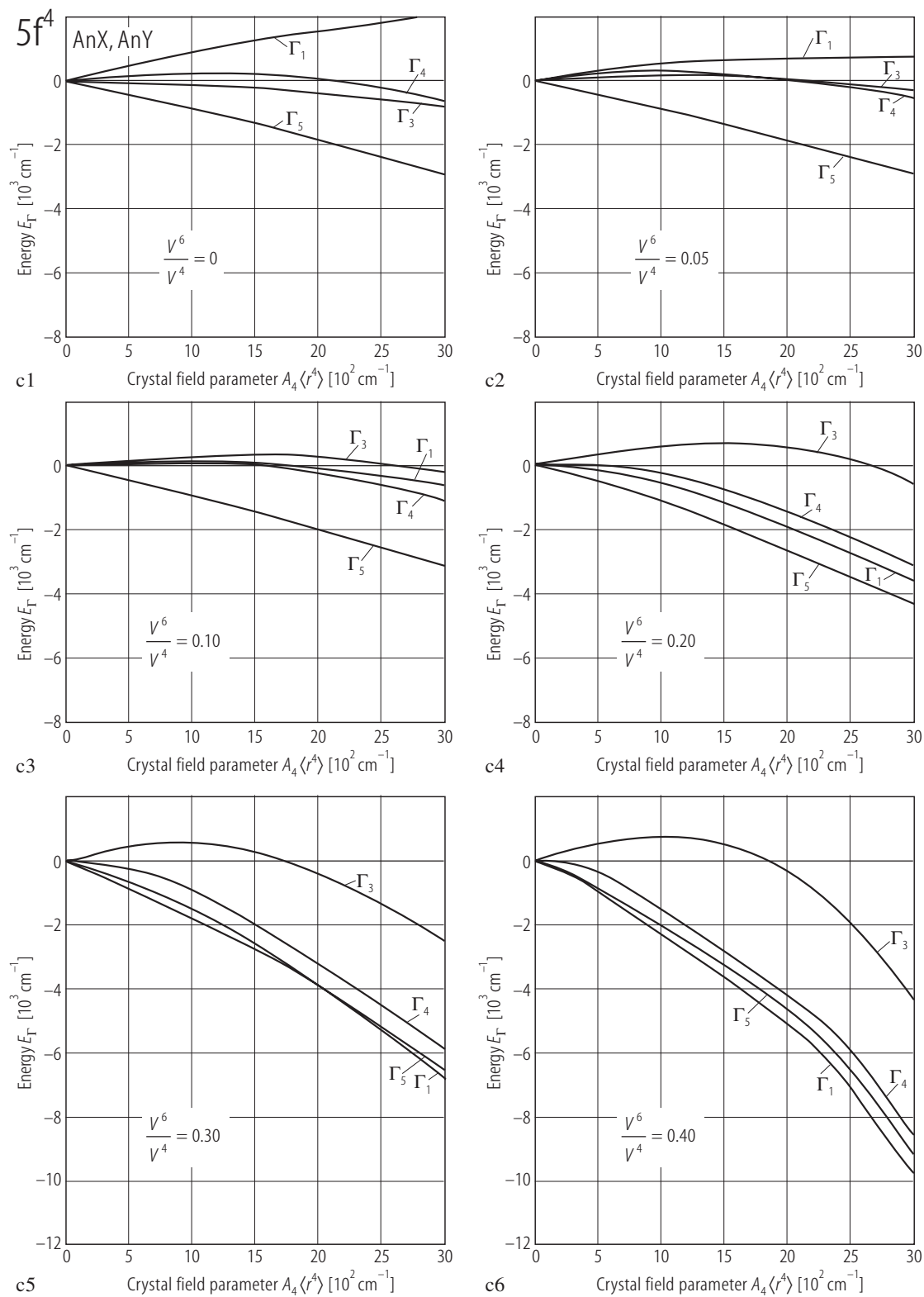
**Fig. R.10.** AnX, AnY. Crystal electric field (CEF) in the NaCl-type actinide compounds. Angular momentum coupling schemes: the Russell-Saunders (R-S) scheme – see Ref. [62LLW], the intermediate coupling scheme [74CL]. The case of light actinides is characterized by the combination of strong spin-orbit (SO) and crystal field interaction causing that an intermediate coupling scheme (IC) rather than the Russell-Saunders (R-S) coupling scheme should be used in the interpretation of magnetic characteristics of actinide compounds. Figures successively present energy-level diagrams for the low-lying states at  $f^2 \dots f^6$  electron configurations. In figures **(a)** ... **(d)** the energy of levels are plotted against the fourth order CF parameter  $V^4 = A_4 \langle r^4 \rangle$  for different ratios of sixth to fourth order parameters  $V^6/V^4$ . As seen, the only quantum number appropriate to characterize the wave function is  $\Gamma$ , the irreducible representation of the point-group symmetry operations. (For further explanations see original papers [70CL] and [74CL]). ↓

For Fig. R.10 see next pages



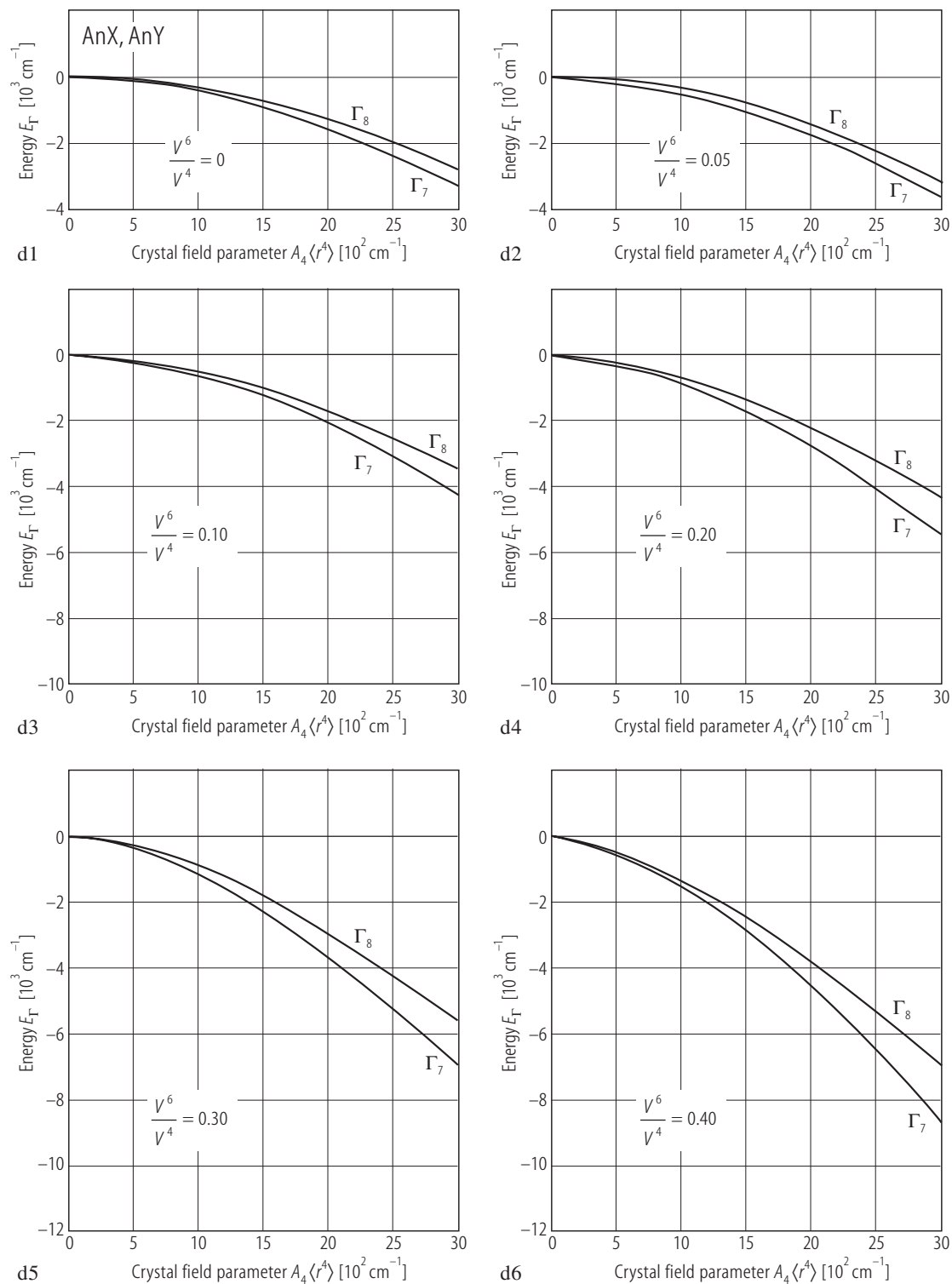
**Fig. R.10a.** For caption see previous page.

$5f^3$ **Fig. R.10b.** For caption see p. 69



**Fig. R.10c.** For caption see p. 69



$5f^5$ **Fig. R.10d.** For caption see p. 69

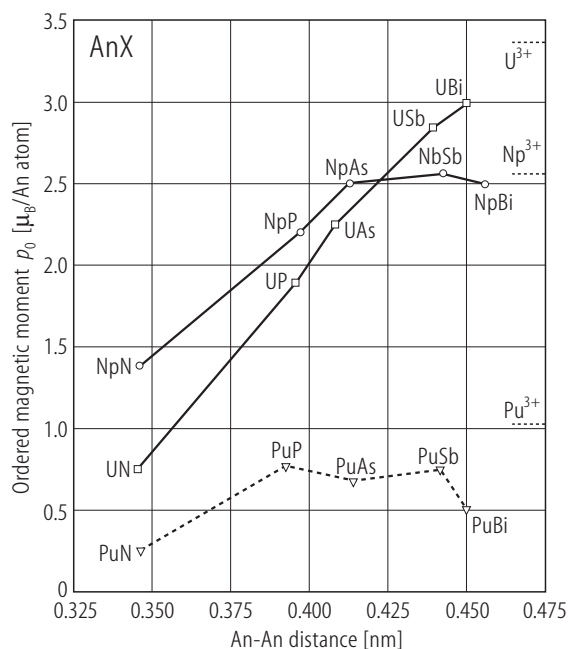


**Fig. R.11.** AnX (An = U, Np, Pu). Ordered magnetic moment,  $p_0$ , vs. the An–An distances. On the far right the  $p_0$  values for the free actinide ions are marked. From various sources.

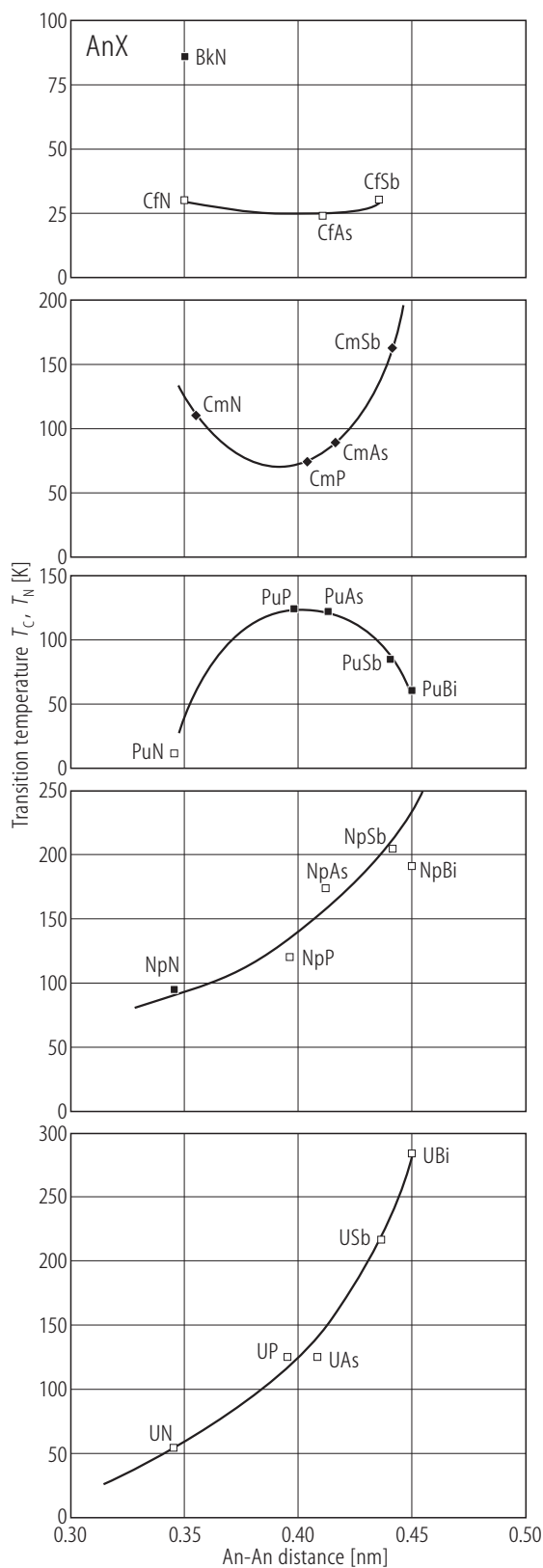


**Fig. R.12.** AnX (An = U, Np, Pu, Cm, Bk, Cf). Transition temperatures:  $T_C$  (closed symbols) and  $T_N$  (open symbols) as a function of An–An distances [87HN].

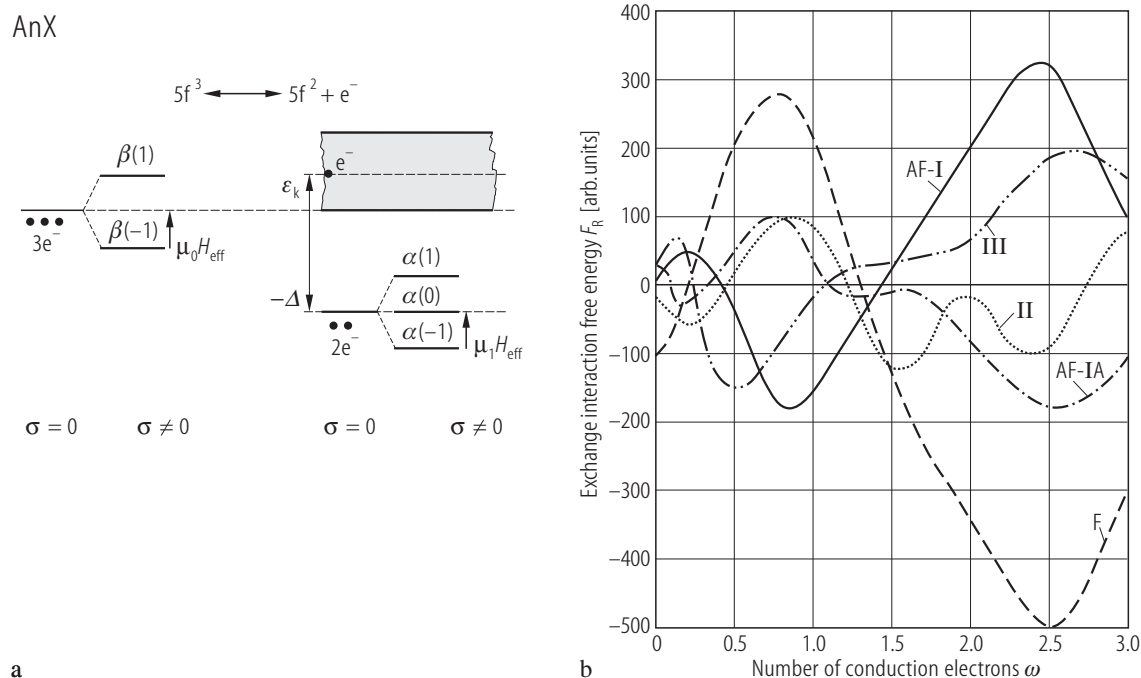


**Fig. R.13.** AnX. Electronic structure and the exchange interactions. Electron delocalization model for actinide rock-salt monocompounds, like (a) UP, UAs, NpC and solid solutions, e.g. U(P,As) and U(X,Y) [73RE], [74RE]. The model adopts the concept that the transition  $5f^n (6d-7s)^2 \rightarrow 5f^{n-1} (6d-7s)^{1+z}$  occurs for a certain fraction of the ions at different temperatures. The transition is induced by the combined effect of either some small energy gap ( $\Delta$ ) or overlap between the  $5f^{n-1}$  localized and itinerant  $(6d-7s)^{1+z}$  states, where  $n = 3$ , the short-range Coulomb interaction between those states (G) and the exchange interaction  $J(p)$  between ions which vary with the occupation of the conduction band (CB). The free energy of these two

different configurations is minimized which yields the temperature dependence of the CB occupation and sublattice magnetization. For further explanation and symbols ( $\Delta$ ,  $\mu_0$ ,  $\mu_1$ ,  $\sigma$ ,  $\alpha(m_1)$ ,  $\beta(m_0)$  and  $\epsilon_k$ ) see the original text.  $H_{\text{eff}}$  is the molecular field, proportional to the magnetization  $\sigma$ . (b) RKKY exchange interaction free energy  $F_R$  (arb. units) of an actinide magnetic ion at a given NaCl lattice site with all other magnetic ions in the lattice as a function of the number of conduction electrons  $\omega$  per magnetic ion (various types of magnetic order, like AF-I, II, III and F are marked) [68GKF]. The types II and III are not observed in the actinide compounds. The curve calculated for AF-IA is added by [73RE].

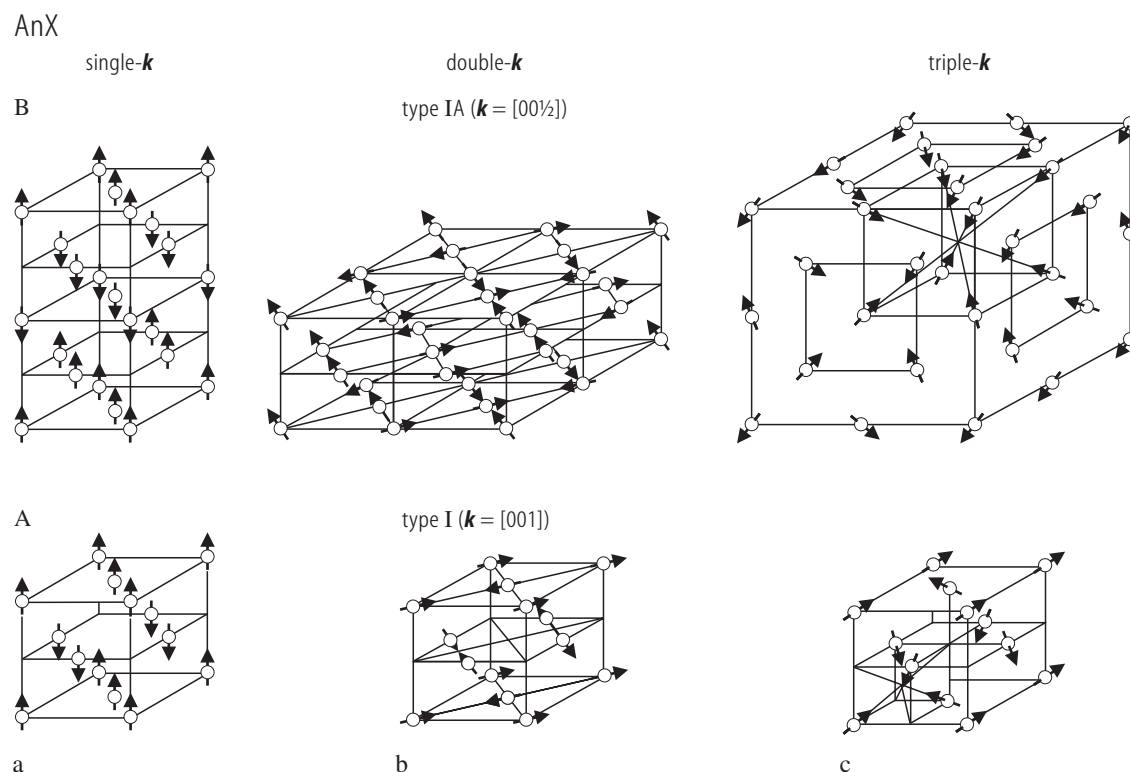


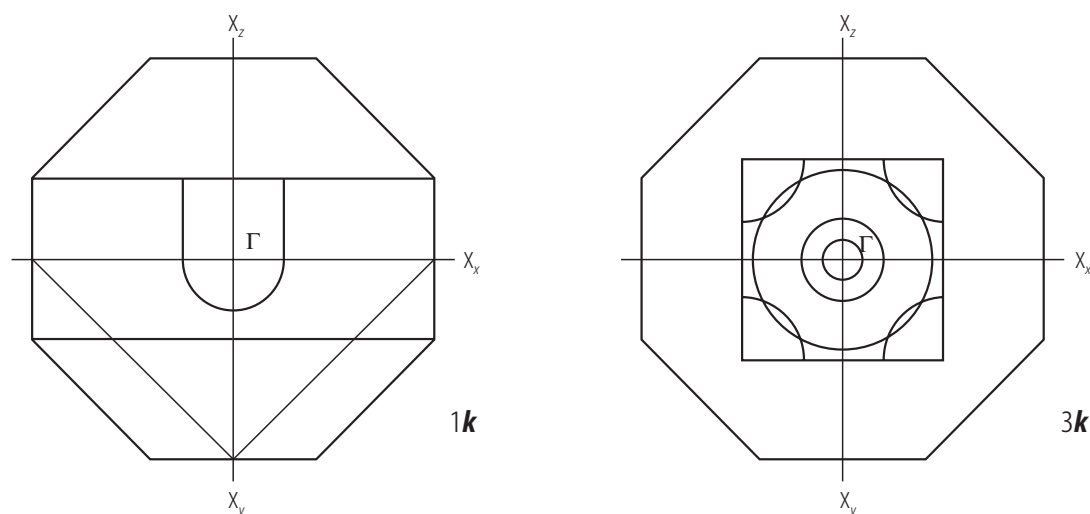
**Fig. R.14.** AnX. Multi- $\mathbf{k}$  magnetic structures associated with the actinide rock-salt structure in the type I (AF I) and type IA (AF IA) phases [86BRQV]. **(A)** AF I: **(a)**  $1\mathbf{k}$ -structure is composed of layers of (001) ferromagnetic sheets, which are antiferromagnetically coupled with the sequence (+-...). A single  $K_z$  domain with  $\mathbf{k}_3 = [001]$  is shown. **(b)**  $2\mathbf{k}$ -structure for single  $K_{xy}$  domains is illustrated by two vectors  $\mathbf{k}_1 = [100]$  and  $\mathbf{k}_2 = [010]$  with the moments along the  $[110]$  direction. **(c)**  $3\mathbf{k}$ -structure is described by three vectors  $\mathbf{k}_1$ ,  $\mathbf{k}_2$  and  $\mathbf{k}_3$  yielding the moments along the  $[111]$  direction. **(B)** AF IA: **(a)**  $1\mathbf{k}$ -structure is composed of layers of (001) ferromagnetic sheets, which are antiferromagnetically coupled with the sequences: (++- -). A single domain  $K_z$  with  $\mathbf{k}_3 = [00\frac{1}{2}]$  is shown. The magnetic moments are directed along the propagation vector  $\mathbf{k}_3$ . **(b)**  $2\mathbf{k}$ -structure is visualized for single- $K_{xy}$  domain as a superposition of two orthogonal propagation vectors  $\mathbf{k}_1 = [\frac{1}{2}00]$  and  $\mathbf{k}_2 = [0\frac{1}{2}0]$  with the moments in the  $[110]$  and  $[1\bar{1}0]$  directions. Symmetry equivalent domains of the form

$K_{yz}$  and  $K_{zx}$  also exists. **(c)**  $3\mathbf{k}$ -structure is composed of three orthogonal propagation vectors  $\mathbf{k}_1$ ,  $\mathbf{k}_2$  and  $\mathbf{k}_3$  and the moments oriented along the  $[111]$  direction. To differentiate multi- $\mathbf{k}$  from single- $\mathbf{k}$  structures one should apply a uniaxial stress or to cool through the phase transition temperature in a large magnetic field (see [87R1]).

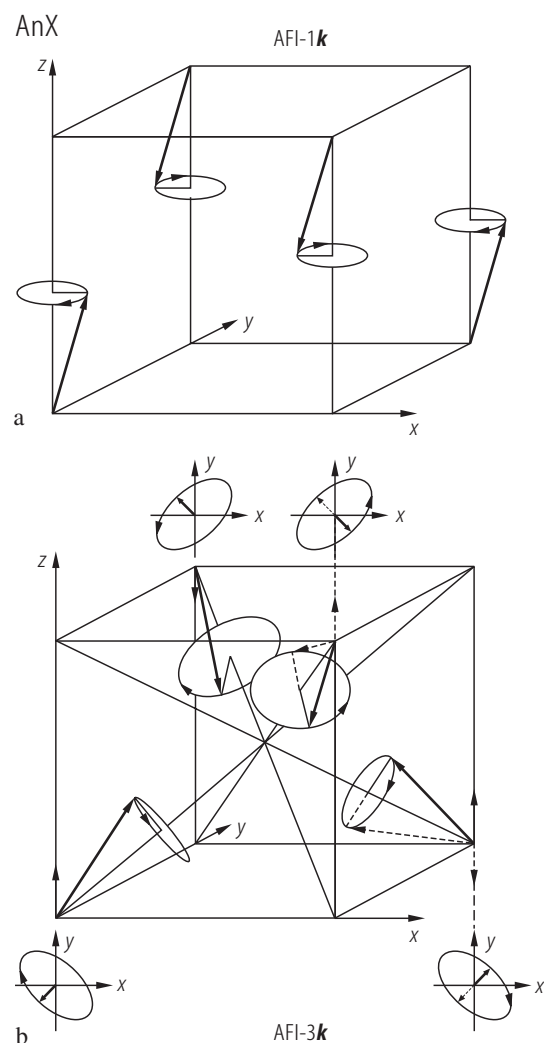
Magnetic moment distribution in the fcc unit cell of the rock salt structure is described by the Fourier expansion:

$$p_n = \sum_{\mathbf{k}} m_{\mathbf{k}} e^{-2\pi i \mathbf{k} \cdot \mathbf{R}_n} \quad (1), \quad \text{where } \mathbf{R}_n \text{ is a lattice}$$

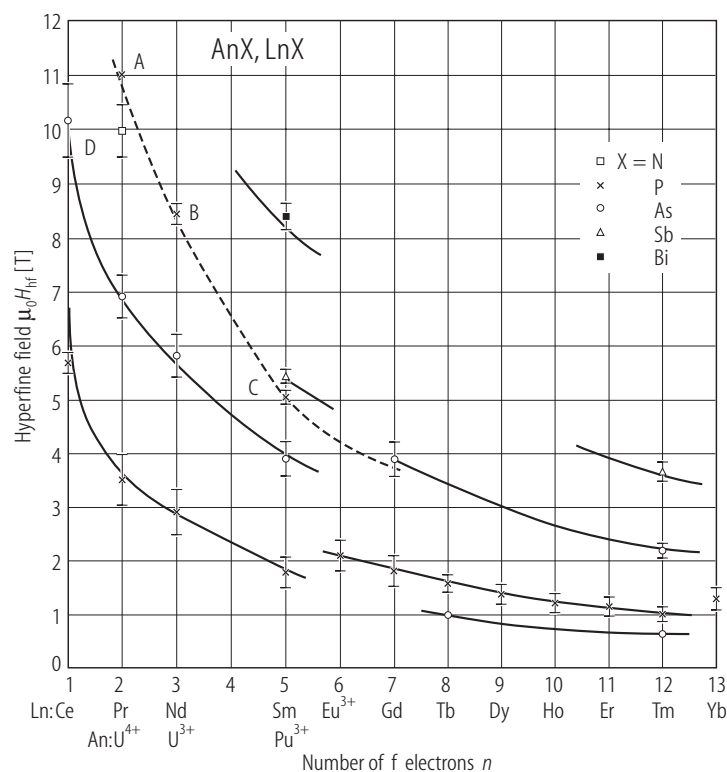
translation,  $\mathbf{k}$  are wave or propagation vectors inside the first BZ and  $m_{\mathbf{k}}$  is the Fourier component which takes a form:  $m_{\mathbf{k}} = \frac{A_{\mathbf{k}}}{2} e^{i\varphi_{\mathbf{k}}} \hat{u}_{\mathbf{k}}$  (2).  $A_{\mathbf{k}}$  is the amplitude,  $\hat{u}_{\mathbf{k}}$  is the unit vector and  $\varphi_{\mathbf{k}}$  is the phase. Note that the neutron diffraction measurements allow to determine only the magnitude and direction of  $|m_{\mathbf{k}}|$ , while the corresponding moment distribution,  $p_{\text{An}}$ , is deduced from eq. (1) [87R1].



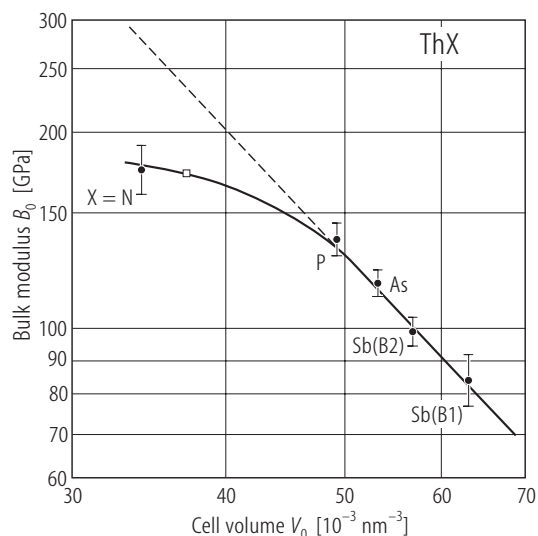
**Fig. R.15.** The initial BZ for the fcc lattice in the paramagnetic state and the reduced BZ's for the  $1k$  or  $3k$ -type AF I structures, drawn as the outer and inner boundaries, respectively. The volume of the BZ is reduced to one-half for the  $1k$ - and one-quarter for the  $3k$ -type of the initial BZ in the paramagnetic state, respectively (taken from [95K2]).



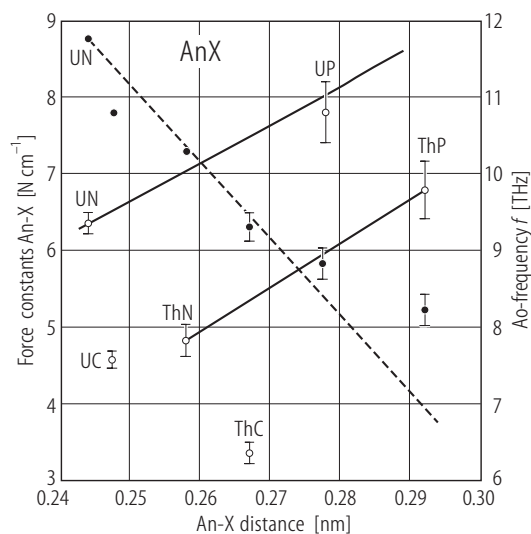
**Fig. R.16.** AnX. Magnetic excitations in the actinide monopnictides. Spin waves in (a) single- $k$  structure and (b) triple- $k$  structure: full and dashed vectors are transverse (T) and longitudinal (L) modes at the zone boundary X, respectively [81JB]. Ellipses show the projections on the  $xy$  planes. In both cases the phases between neighbour planes are  $180^\circ$  out of phase. Hence, in the L mode the transverse components cancel each other and are not observed in neutron diffraction experiment (compare Fig. V.42), while the longitudinal components are in phase within each layer and the longitudinal mode is detected by neutrons. This explains surprising features of the observation in USb at low frequency by only a longitudinally polarized mode L (modulation along the quantization axis [111]) than the precession of the magnetic moment around the quantization axis (transverse excitation T) [78LSSV]. The second T mode is at higher energy. Both these results agreed with neutron inelastic experiments of USb (see Fig. V.50) and giving proof that the magnetic structure, e.g. of USb, is of the triple- $k$  form.



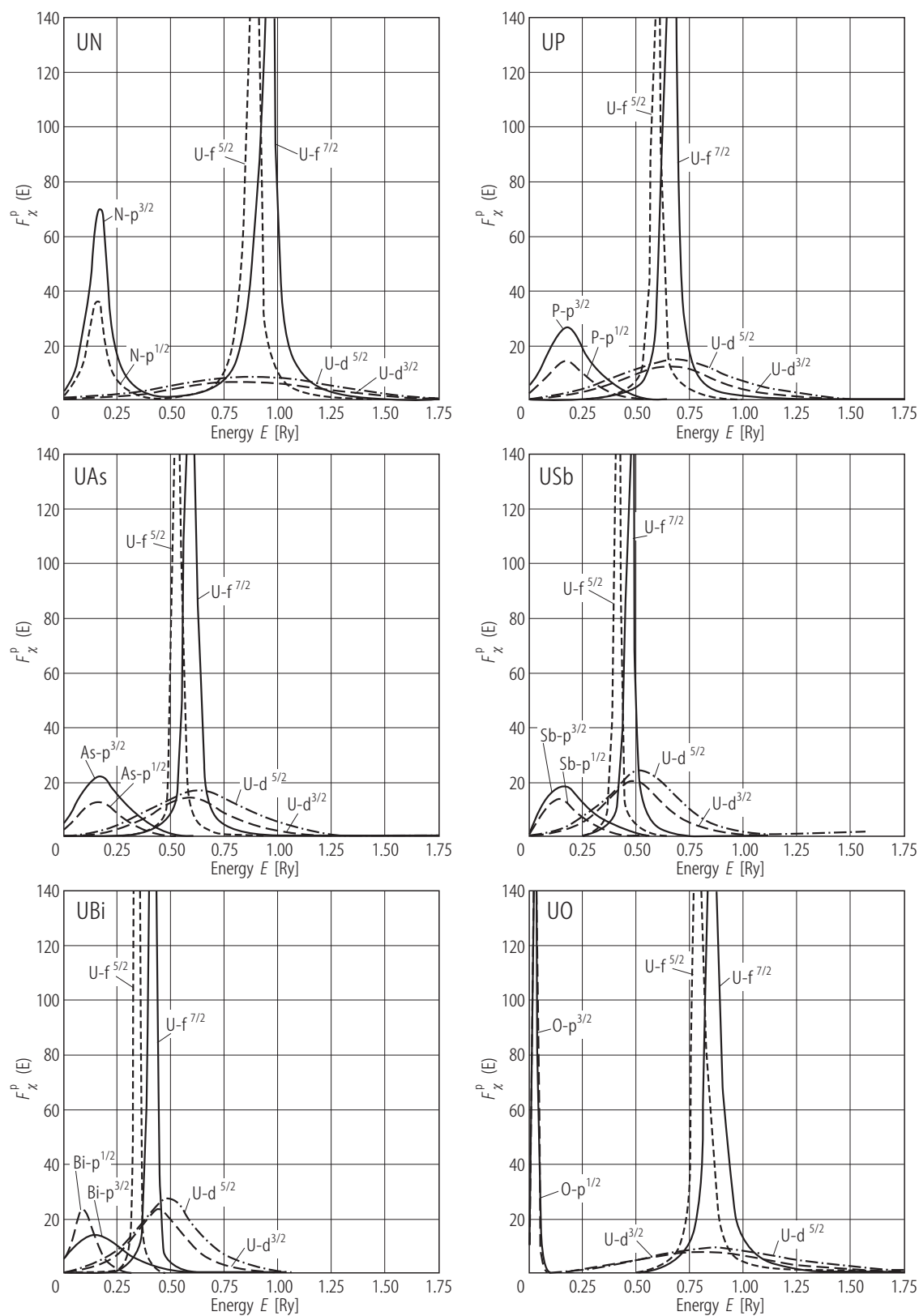
**Fig. R.17.** AnX, LnX. A plot of the NMR line-shift results on actinide mononpnictides AnX compared to the results on lanthanide monocompounds LnX [71FG]. In the figure there is plotted the (super) hyperfine field  $H_{hf}$  per unit spin on each of the six paramagnetic ion neighbours as a function of the number,  $n$ , of f-electrons.  $H_{hf} = g_J N \alpha \mu_B / (g_J - 1)$  ( $g_J$ -Landé factor,  $N$  is the Avogadro number,  $\alpha$  is a function of the number of electrons in the f-shell). Point A is for  $U^{4+}P$  ( $g_J = 0.8$ , Russell-Saunders coupling), point B for  $U^{3+}P$  ( $g_J = 0.766$  using intermediate coupling) [69LFG], point C is for  $Pu^{3+}P$  ( $g_J = 0.286$ ) [69LFG] and point D is for  $U^{4+}N$  ( $g_J = 0.8$ , Russell-Saunders coupling [69K]). Data for LnN are taken from [62SW] and for Ln(P...Bi) from [69J].



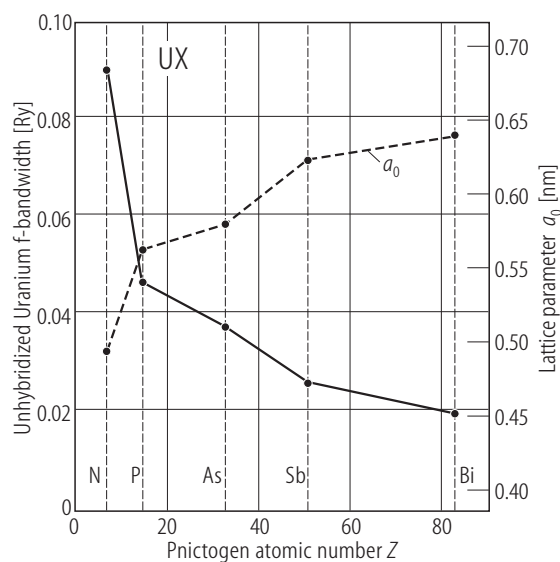
**Fig. R.18.** ThX (X = N...Sb). A log-log plot of bulk modulus,  $B_0$ , vs. volume,  $V_0$ , per formula unit [88GSBD]. The slope of the straight line passing through experimental points (except for ThN) is  $-2.05(15)$ . Note that  $B_0$  for ThN is considerably lower than one should expect from the  $-2$  power law, but is in consistency with the theoretical result (open square) given in [84B3].



**Fig. R.19.** AnX (An = Th, U; X = C, N, P). An average optical (Ao) frequency (closed circles – rhs) and the An–X bonding force constants (open circles-lhs) against the An–X distances ( $a_0/2$ ) [74W]. The dashed and solid lines are guides for the eye. Note that the force constants for the UX compounds are about 20...30 % higher than those for corresponding ThX compounds, with the exception of the carbides ThC and UC for which these constants are anomalously low. Unexpectedly, the uranium and thorium data of optical frequency (OF) fall approximately on the same straight line (dashed line) with small deviation for UC and somewhat larger one for ThP.

**Fig. R 20.** For caption see next page.

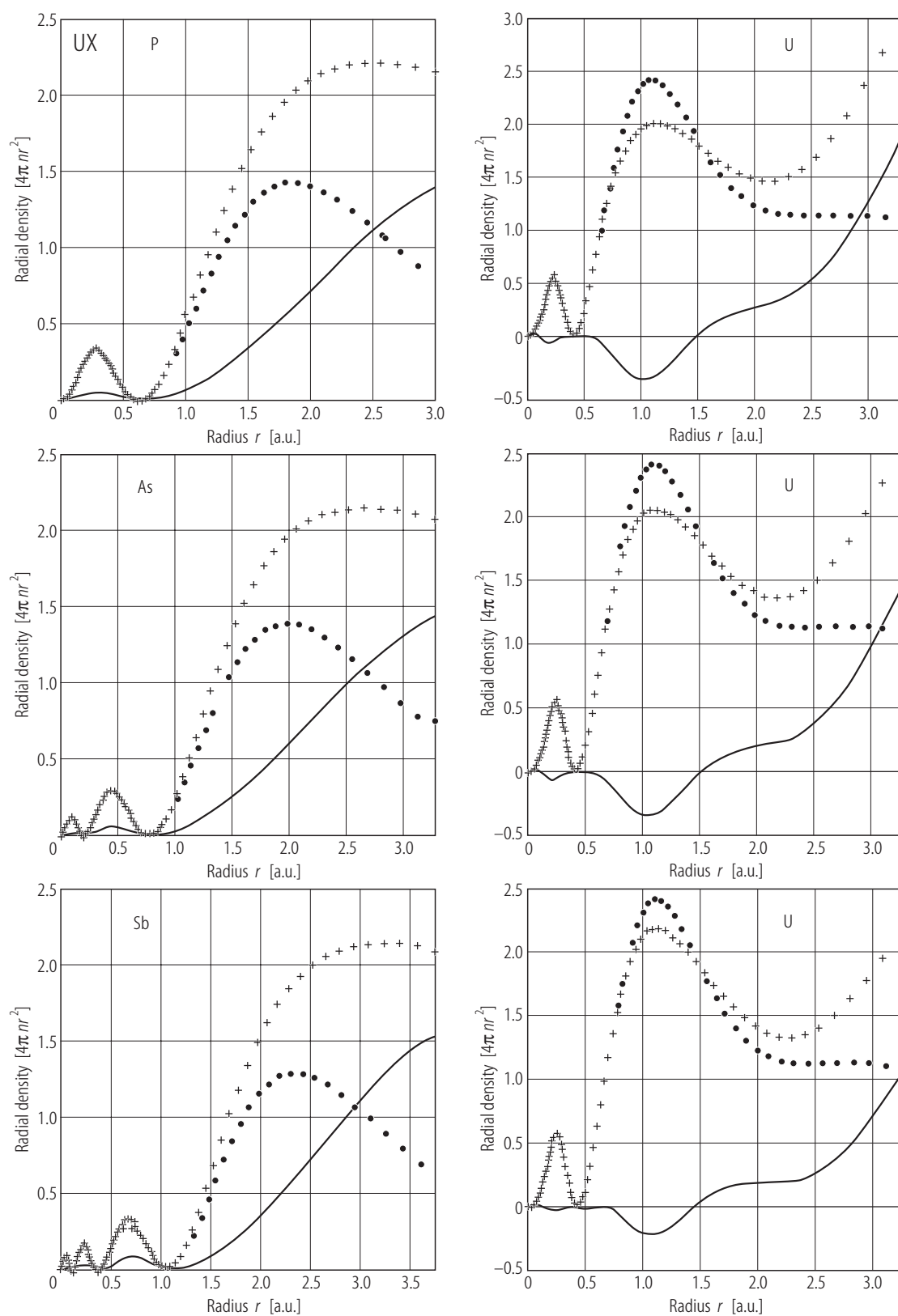
**Fig. R.20.** UX (X = N...Sb, O). Electronic structure using a fully relativistic single-site scattering (RSSS) model [79MW]. Resonant  $\chi$ -like differential Friedel summands for uranium and the non-metals. The calculations indicate that the U 5f-electrons form a narrow well-localized band. Due to the overlapping of the uranium and the non-metal resonances, the bonding between uranium and non-metal constituents has considerable covalent character. This increases with atomic number and is mostly important for the heavier representants of group V elements. The separation  $f^{5/2}-f^{7/2}$  is constant and independent of the non-metal component.

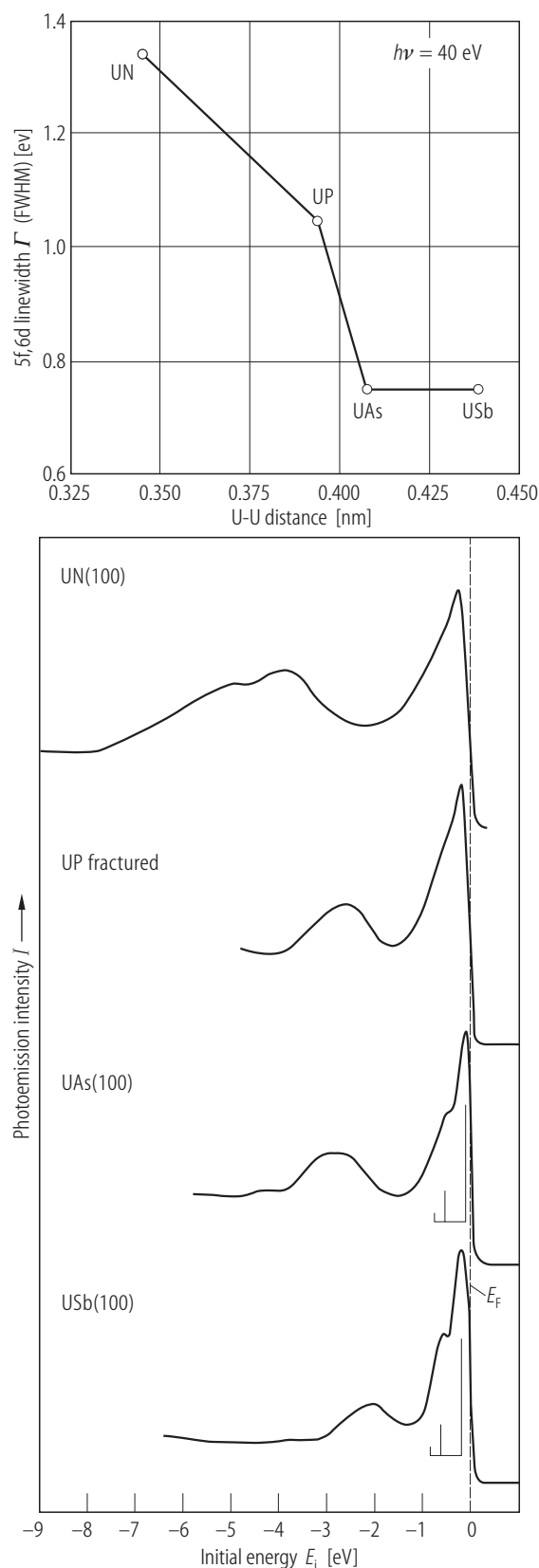


**Fig. R.21.** UX (X = N...Bi). Unhybridized uranium bandwidth, calculated by the LMTO method using LDA and  $f^2d^2s^2$  configuration of uranium for the entire UX series (lhs) and lattice parameters  $a_0$  (rhs) marked by solid and dashed lines, respectively [79AB]. The former is of particular significance since this is a measure of the localization of the f-electrons. This in turn determines the extent to which correlation effects, neglected in band structure calculations, might be important. Note a clear correlation between the variation in lattice parameter and f-bandwidth, supporting the earlier suggestions of [74D], that the observed f-band narrowing with increasing the pnictogen atomic number Z is mainly due to the increasing in  $a_0$ -values.

**Fig. R.22.** UX (X = P, As, Sb). Radial charge densities ( $4\pi nr^2$ ) of the uranium monopnictides in the free atom (dots) and solids (crosses) at the Wigner-Seitz sphere boundary. The charge densities in the uranium and pnictogen spheres are given in right and left panels, respectively, by using the LMTO ASA method [84B2]. The difference between free-atom and solid-state charge densities is shown as solid curve. The systematic decrease of bonding charge across a pnictide series is essentially due to a volume effect.

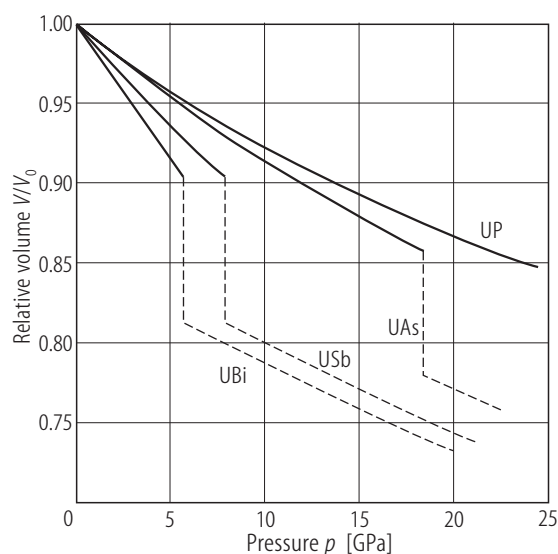


**Fig. R.22.** For caption see previous page.

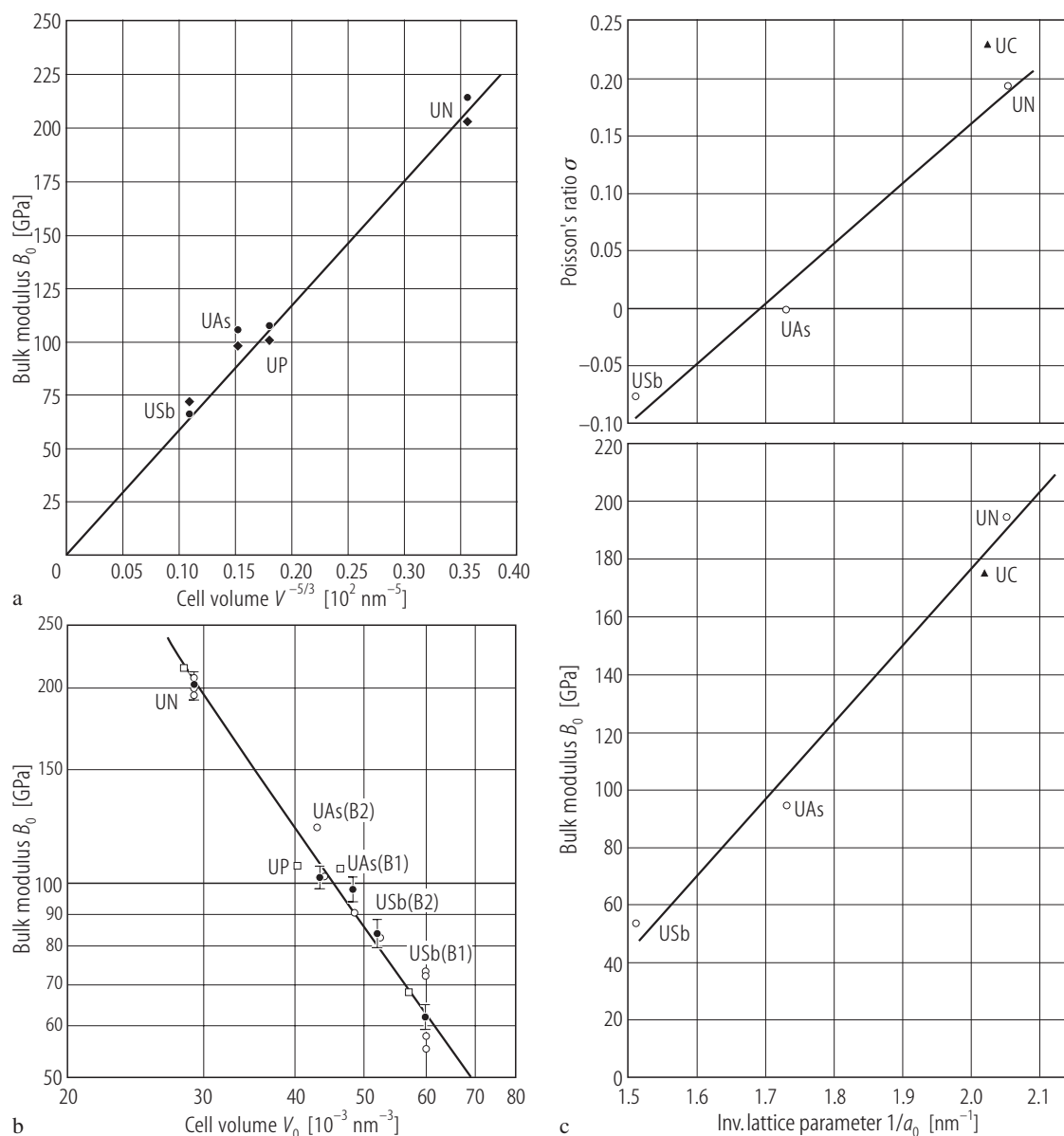


←

**Fig. R.23.** UX (X = N...Sb) s.c. Photoemission spectra at  $h\nu = 40$  eV from the surface cleaved along the (100) plane of UN, UAs and USb single crystals. Polycrystalline UP was fractured [87R2]. As indicated by the bar diagrams for UAs and USb the 5f emission feature corresponds to a  $5f^2$ -final state multiplet. This clearly points to a  $5f^3$  ground state configuration at least for USb. The upper figure shows FWHM ( $\Gamma$ ) of the 5f and 6d feature at  $E_F$ . The decreasing of  $\Gamma$  with increasing U-U spacing along the pnictogen column is evident owing to the reduced 5f overlap with the ligand electrons.



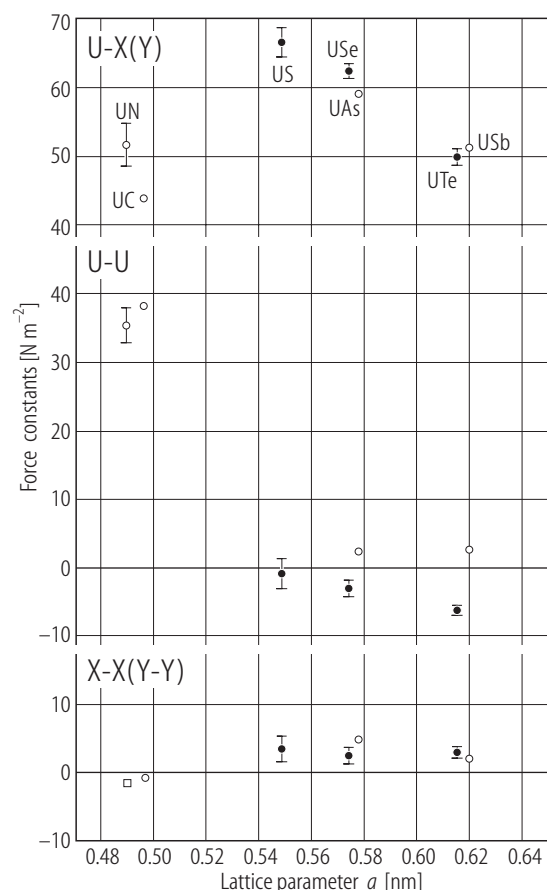
**Fig. R.24.** UX (X = P, As, Sb, Bi). Relative volume,  $V/V_0$ , vs. pressure,  $p$ , up to about 25 GPa [93L1, 93GHBH]. For this pressure range only in the case of UAs, USb and UBi a change from B1 (NaCl - type) to B2 (CsCl - type) structure takes place at 17, 7 and 5 GPa, respectively. This transition involves a change of coordination for the metal atom from 6 to 8. All three cases show a hysteresis effect (not shown here) upon the release of pressure. The difference in the critical pressures  $p_t$  is attributed to the main interactions of f-d or f-f type in UP and UAs decreasing along the series and starting domination of the f-p type interaction in USb and UBi. One should, however, take into account the fact that the largest U-U distance in UBi at ambient pressure, compared to the other uranium monopnictides, at the maximum pressure applied, drops into that of Hill critical zone. The volume changes for UAs (11%), USb (11.6 %) and UBi (11%) at the corresponding transition pressures are considered as being due to the delocalization processes of their 5f electrons and following charge transfer, which are directed oppositely to the repulsive forces between ions, which in turn help in the volume collapse (see [03JS]). On the other hand, ThSb [88GSBD], having no f electrons, has a similar B1-B2 structure transition to that of USb. The only difference is that ThSb does not retain the B2 high-pressure phase as a metastable form. It is likely that anion-anion interactions (second neighbours) in these monopnictides play a major role in determining their phase behaviour under pressure



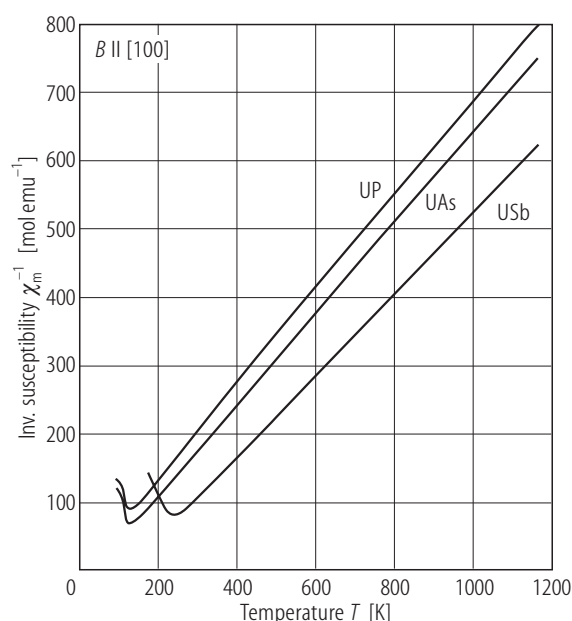
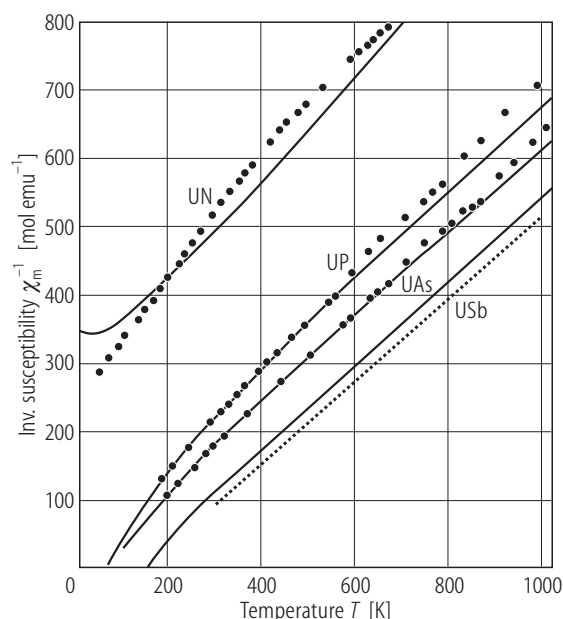
**Fig. R.25.** UX (X = C, N, As, Sb). **(a)** Bulk modulus,  $B_0$ , as an inverse function of the 5/3 power of the unit cell volume  $V$  [86LORV], as expected for metallic or covalent bonding. Closed circles are theoretical values from Refs. [84B2] and [84B3]. Closed diamonds are experimental values from Refs. [84B4], [85SGB], [86SGBI] and [86VRL]. **(b)** A log-log plot of bulk modulus,  $B_0$  vs. cell volume per formula unit,  $V_0$  [89SGBD]. B1 has NaCl-type while B2 has CsCl-type structure. Closed and open circles are experimental data from [85SGB] and [88SGBD], respectively

which are compared to the theoretical values (open squares) of [84B2] and [84B3]. The slope of the line passing through the data points is  $-5/3$  as expected from a free electron theory of simple metals. This confirms the earlier findings of [86LORV]. See also a review given in [93L1]. **(c)** Poisson's ratio,  $\sigma$ , and bulk modulus,  $B_0$ , as a function of inverse cell parameter  $1/a_0$  of uranium monopnictides determined from the low  $q$  neutron scattering data [83BHJM].

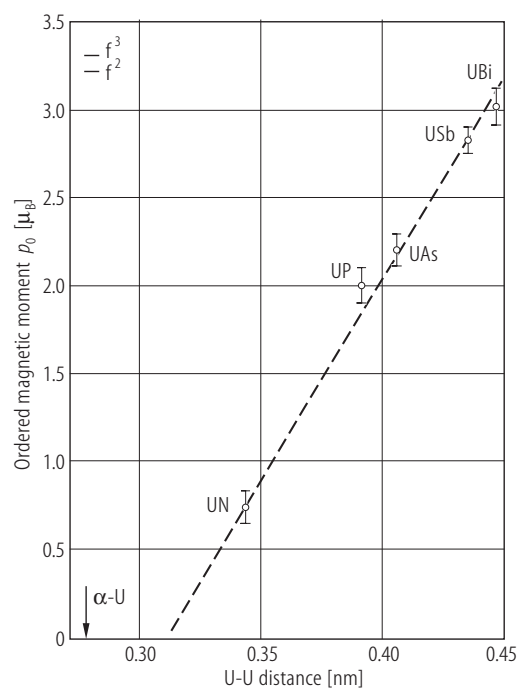
**Fig. R.27.** UX (X = N...Sb). Inverse molar magnetic susceptibility,  $\chi_m^{-1}$  vs. temperature,  $T$ , up to 1000 K [84T]. The solid lines represent the CEF calculations: for UN [78LL2], UP, UAs [74TL] and USb [84T].



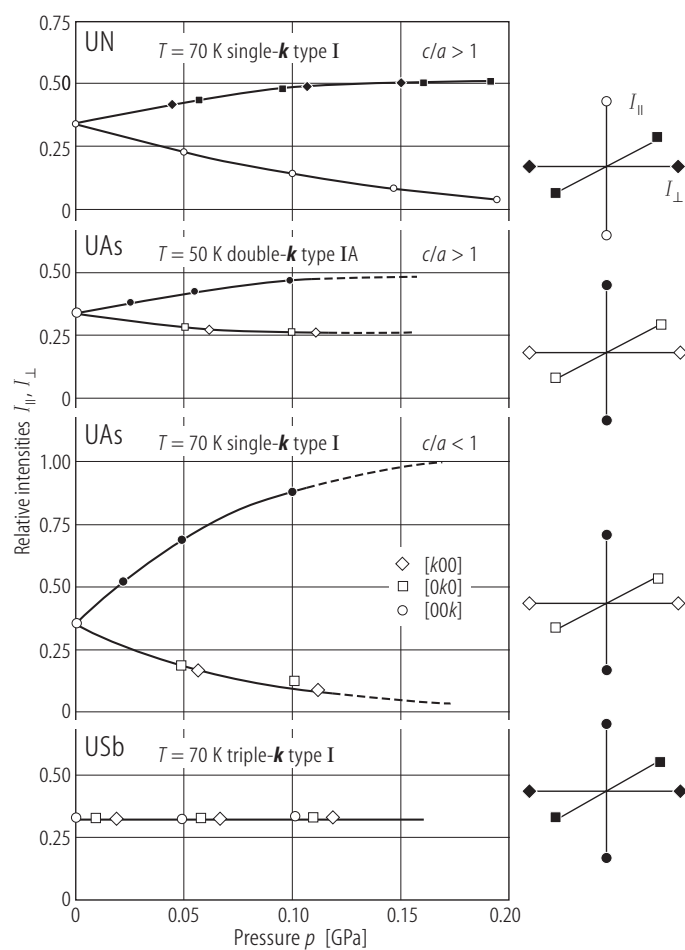
**Fig. R.26.** UX, UY. The effective radial force constants determined by fitting the rigid-ion and shell models to experimental dispersion relations [86JHBD]. Note that the U–X (Y) force constants are dominant and almost invariant along the series, while the remaining U–U and X–X (Y–Y) force constants have magnitudes close to zero (except for those in UC and UN). The large magnitudes of the U–U force constants in UC and UN are due to the overlap of the most extended 6d electrons, while for the other members of the series the d–d repulsive contribution is considerably reduced due to the large U–U separation.



**Fig. R.28.** UX (X = P, As, Sb) s.c. Inverse magnetic molar susceptibility,  $\chi_m^{-1}$ , vs. temperature,  $T$ , up to 1200 K obtained on  $B \parallel [100]$  single crystal orientation [79BHV]. Diamagnetic corrections (UP:  $-64$ , UAs:  $-83$ , USb:  $-105 \cdot 10^{-6}$  emu/mol) were applied. Good agreement was found with powder measurements of UP and UAs by [74TL]. For USb a perfect straight line could be fit between 300...1200 K with  $p_{\text{eff}} = 3.64 \mu_B$  and  $\Theta_p = 140$  K. For UP and UAs the results are interpreted in the framework of intermediate crystal electric field (CEF)-treatment (see [74TL]) with  $5f^3\Gamma_8^{(2)}$  ground state. In the case of USb,  $5f^3\Gamma_8^{(1)}$  ground state has been assumed from the form factor study [76LMSV].

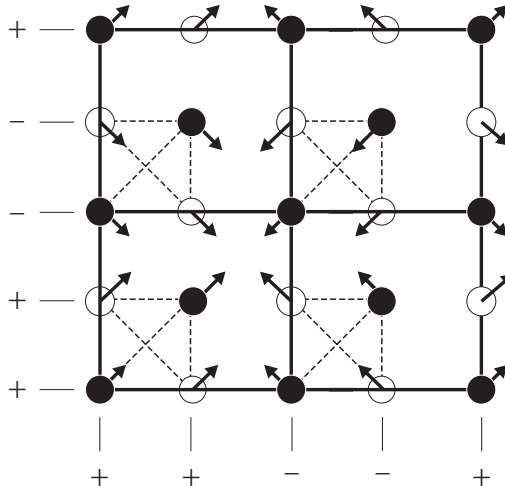
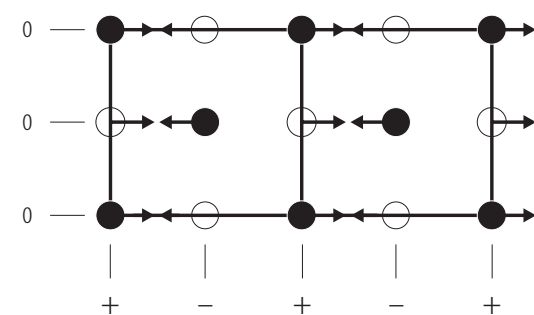
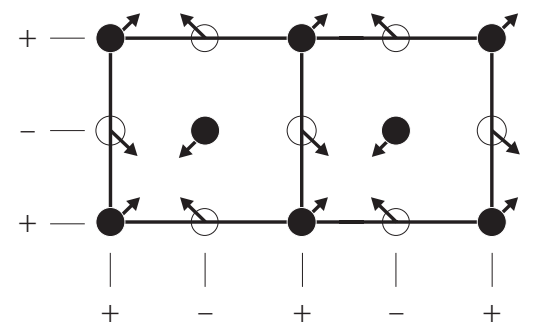
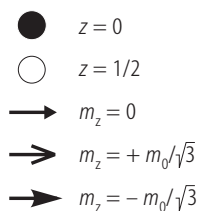
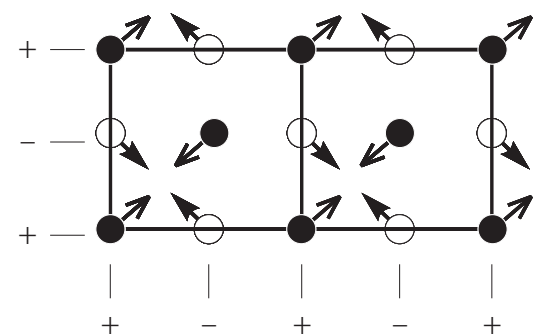


**Fig. R.29.** UX (X = N...Bi). Ordered moment of uranium,  $\rho_0$ , vs. the U-U separation for uranium monopnictides [80SLV]. The free ion values of  $U^{4+}(5f^2)$  and  $U^{3+}(5f^3)$  are marked. The U-U distance for nonmagnetic  $\alpha$ -U is also marked by the arrow.

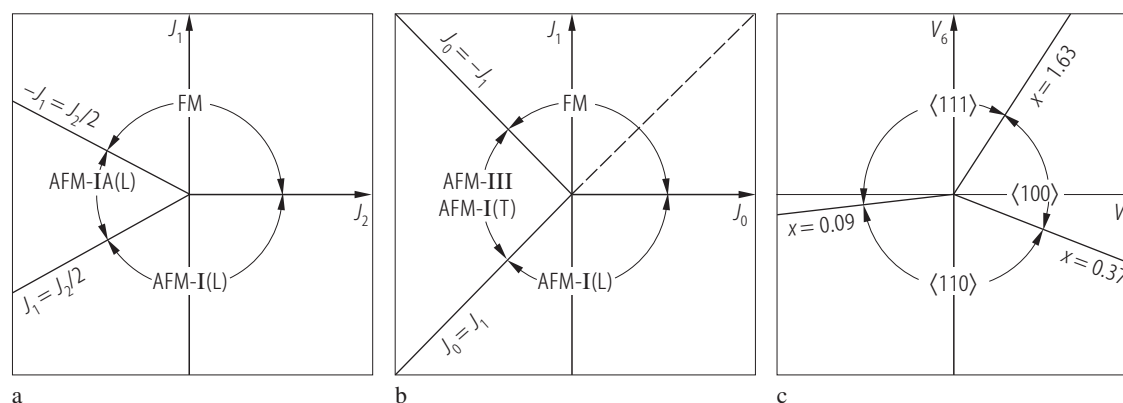


**Fig. R.30.** UX (X = N, As, Sb) s.c. Relative intensities of Bragg peak,  $I_{||}$ ,  $I_{\perp}$ , vs. an uniaxial pressure applied along the [100] direction [80RBQV]. Only magnetic peaks represented by filled symbols remain after domain reorientation. Closed circles correspond to the intensity of magnetic peaks contributing to  $I_{\perp}$  ( $k \perp [100]$ ) and open circles to those contributing to  $I_{||}$  ( $k \parallel [100]$ ). The observed increase of given intensity with increasing uniaxial stress allows to derive the proper magnetic structure of  $1k$  or  $2k$  type. The lack of any change gives evidence about a multiaxial  $3k$  structure. For details see the original paper.

UX

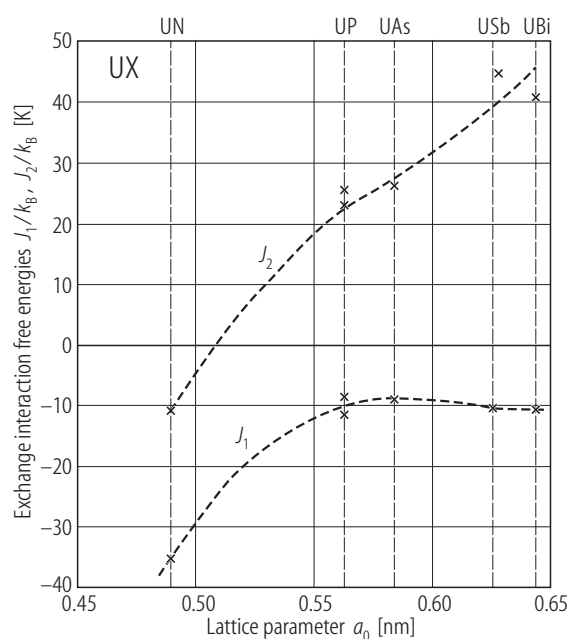
AFI  $\mathbf{k} = [1,0,0]$ AFIA  $\mathbf{k} = [1/2,0,0]$ single- $\mathbf{k}$  UN, UP, UAs(HT)double- $\mathbf{k}$  UAs(LT)double- $\mathbf{k}$  UP(LT)triple- $\mathbf{k}$  USb

**Fig. R.31.** UX. Projection of magnetic moment arrangements AF I and AF IA onto the basal plane (001) for all magnetic structure types existing for the uranium mononictides [96MGBV].

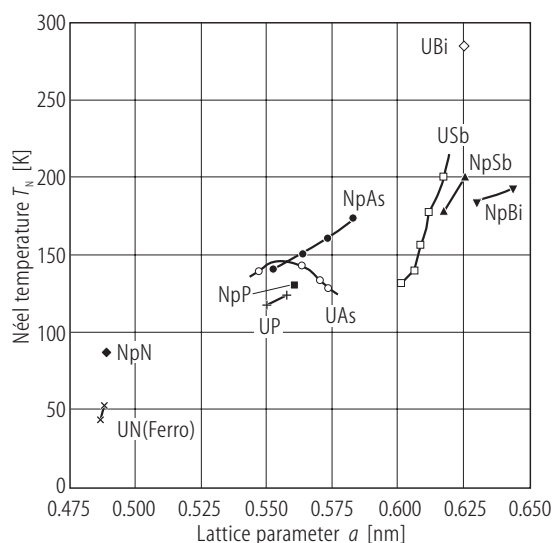


**Fig. R.32.** UX. The stability diagrams for the fcc longitudinal (L) and transverse (T) magnetic structures in terms of the (nn) interaction parameters:  $J_0$  for spin components perpendicular to the face plane and  $J_1$  for spin components parallel to this plane, as well as to the coupling constants for (nnn), i.e.  $J_2$  for spin components parallel to the line joining the two atoms and  $J_3$  for spin components perpendicular to this line [83MW]. Diagram (a) arises with setting  $J_2 = J_3 = 0$  in the expression for the exchange energy (see the original paper). The (L) AF I structures of UN, UP and USb are contained in the half-plane  $J_0 - J_1 > 0$ . Diagram (b) arises with  $J_0 - J_1 > 0$  (longitudinal structures), where  $J_0$  is positive and  $J_3 = 0$ . Here the AF type IA of UAs and type I phases corresponding to UN, UP and USb are stable.

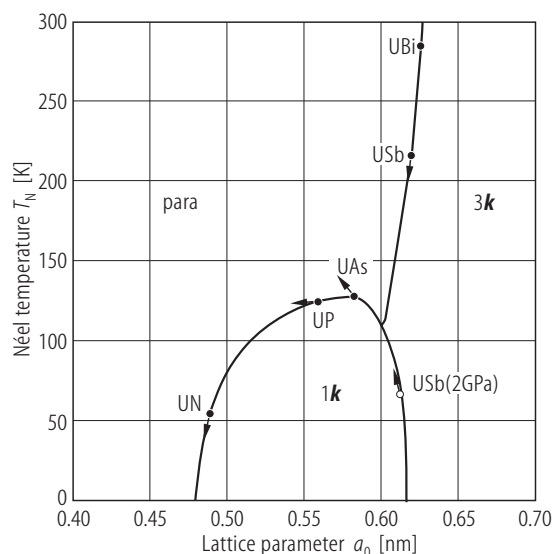
However, the single- and multiple  $k$ -structures are degenerate if the crystal field is not taken into account. This means that single- and multiple- $k$  structures have the same exchange energy. Diagram (c): the sign and the relative magnitude of crystal field parameters  $V_4$  and  $V_6$  determine the spin directions, where  $B_4 = \beta V_4$  and  $B_6 = \gamma V_6$ . The magnetic structures of UN, UP (LT) and USb are understandable if their crystal-field energy has a minimum in the  $[100]$ ,  $[110]$  and  $[111]$  directions, respectively. In the case of UAs (LT) its crystal field energy minimum is at the  $[110]$  direction and exchange parameters correspond to diagram (b). Introducing an anisotropic term of tetragonal symmetry in the exchange interactions lifts the degeneration of two kinds of multiaxial structures [86M].



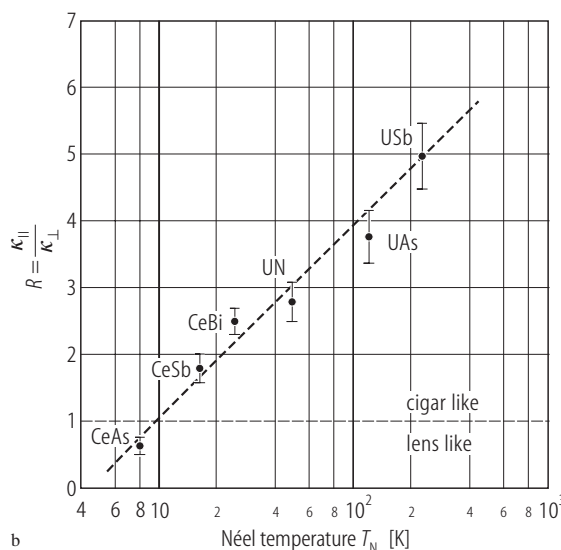
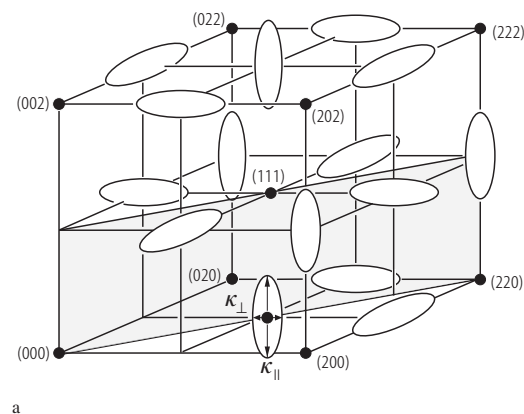
**Fig. R.33.** UX (X = N., Bi). The exchange interaction constants,  $J_1$  and  $J_2$ , derived by an analysis of the experimental results ( $\Theta_p/T_N$ ) using the molecular-field theory (MFT) as a function of lattice parameter  $a_0$  [68GKF]. The  $J_1$  and  $J_2$  magnetic-exchange constants describe the nearest-neighbour (nn) – and the next nearest-neighbour (nnn) – interactions, respectively. The two types of interaction mechanism are postulated, namely 1) RKKY and 2) superexchange (SE) mechanisms, then  $J_i = J_i(\text{RKKY}) + J_i(\text{SE})$ ,  $i = 1, 2$ . For the RKKY-type interaction, one would expect  $J_i$  to be large for small  $a_0$  and to decrease rapidly and finally to saturate to a constant value for large  $a_0$ , as is the case for  $J_1$ , but not for  $J_2$ , which changes its sign and it does not level out for large  $a_0$ . This is probably due to the presence of a strong  $180^\circ$  cation-anion-cation superexchange interaction in addition to the RKKY mechanism, which lowers  $J_2$  to a negative value. See also the molecular field approximation expanded to the tenth nearest neighbours derived for these monopnictides [70AI].



**Fig. R.34.** UX, NpX (X = N...Bi). The ordering temperature vs. lattice parameter  $a(p)$  for all uranium and neptunium monopnictides [98BDGI]. There is a correlation between the pressure dependence (diminishing of the lattice parameter) of the ordering temperature and the type of magnetic structure. For example the triple- $k$  compounds USb and NpSb show very strong negative pressure dependences of their  $T_N$  with  $p$  inspite of almost localized behaviour.



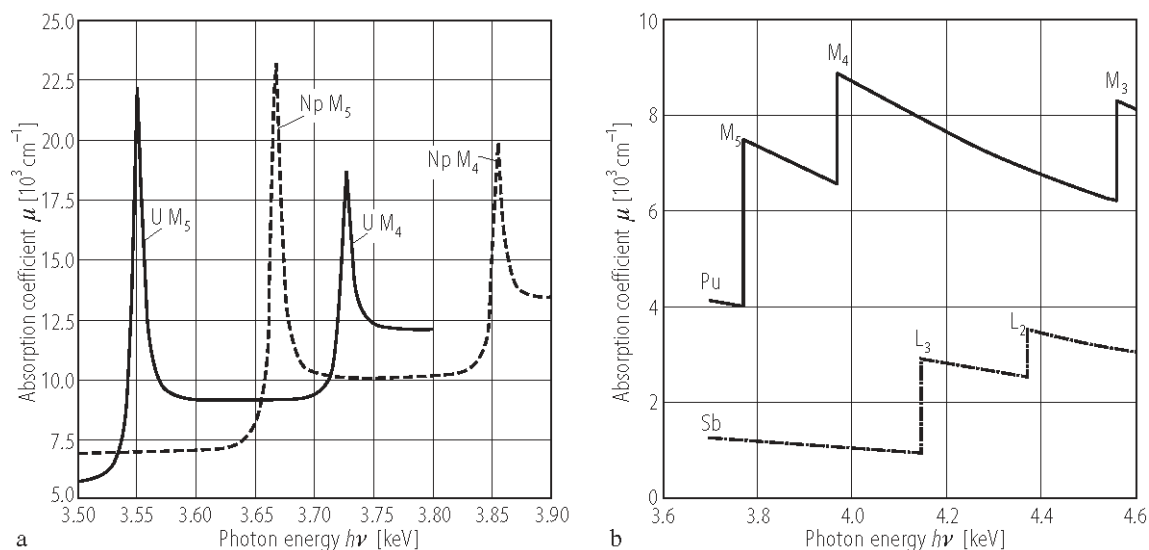
**Fig. R.35.** UX (X = N, P, As, Sb, Bi). Magnetic phase diagram,  $T_N$ , vs. lattice parameter,  $a_0$ , for the uranium monopnictide series [96BGMO]. The low-temperature magnetic phases for UP and UAs are omitted. The arrows point to the direction of changes in the lattice parameter derivative at  $T_N$  for  $p = 0$ . Note the appearance of a high-pressure (above 2 GPa) and low-temperature ( $T_1 < 65$  K)  $1k$ -phase of USb (see Fig. V.38) except for the well known  $3k$ -phase.



**Fig. R.36.** UX, UY. **(a)** The diffuse critical neutron scattering (DCNS). The reciprocal space for  $T > T_N$  diffuse neutron scattering in the AF-I centers with anisotropic cigar like inverse correlation lengths  $\kappa_{||}$  and  $\kappa_{\perp}$ , parallel and perpendicular to the spin direction [84HF], [86HF]. For example,  $\kappa_{||}/\kappa_{\perp} = 5.0(5)$  for USb. This anisotropic correlation behaviour above  $T_N$  is direct evidence for the existence of anisotropic magnetic interactions in the cubic monopnictides. The shaded area represents an interaction plane **(b)** The correlation ratio,  $R = \kappa_{||}/\kappa_{\perp}$ , vs.  $\log T_N$  for the CeX and UX

series [84HF]. The thick dashed line suggests a logarithmic law in the correlation lengths ratio  $R$  and  $T_N$ . The thin horizontal dashed line separates out the distribution observed with different shapes of intensity. For experimental  $R$ -values in Np and Pu monopnictides see [91LA] (see Fig. IV.105). Note that the anisotropy of the correlation lengths diminishes on going from the UX to CeX system and towards lighter pnictides. The explanation of this tendency was given in [86KC2].

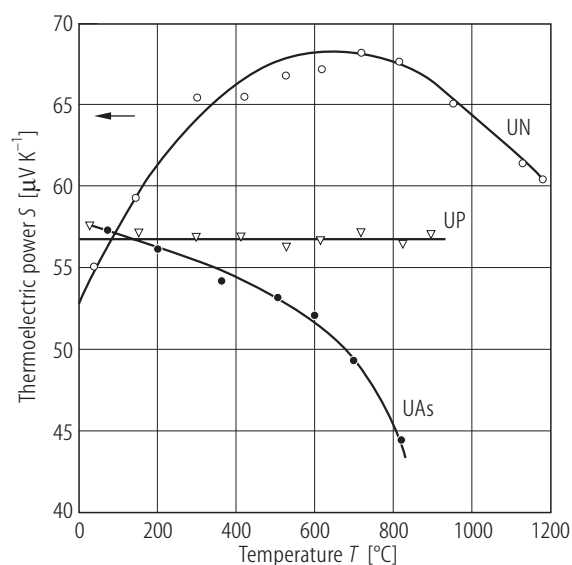




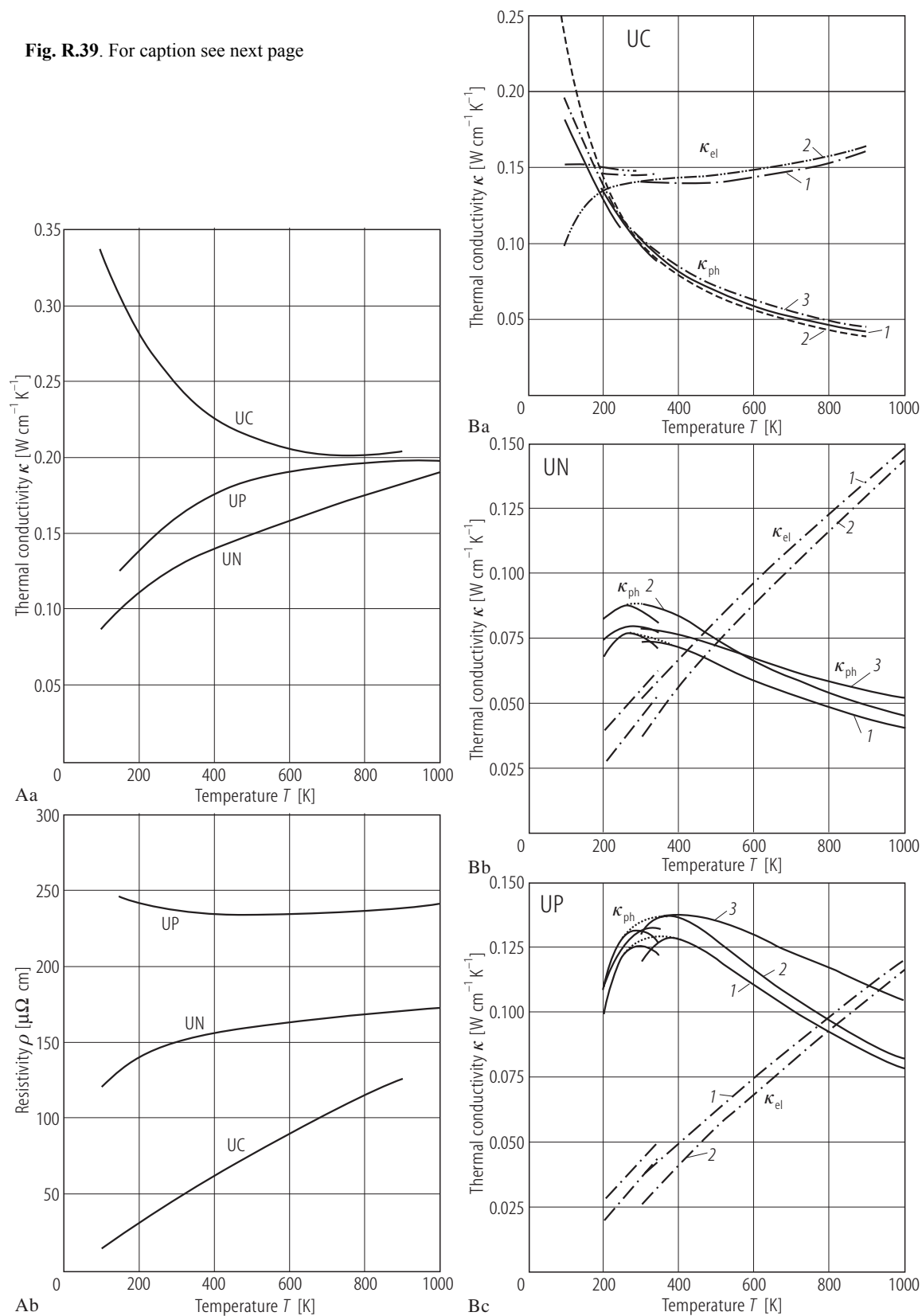
**Fig. R.37.** U, Np, Pu. RXMS: The absorption coefficient,  $\mu$ , for (a) U and Np [94LSLR2] and for (b) Pu (cited at [99MLLR]) as a function of photon energy  $h\nu$ . Note the maxima at the resonant energies of  $M_{4,5}$  edges:

	$M_4$ [eV]	$M_5$ [eV]
U	3723	3548
Np	3852	3666
Pu	3964	3768

The increase in energy between U, Np and Pu is caused by the increase in nuclear charge. The differences in the resonance energies imply that the individual moments on different actinides can be determined, for example, in solid solutions, which is not possible with neutrons (see the case of (U,Pu)Sb in [02NSML2]). The ratio of amplitudes  $A_4$  and  $A_5$  determines the so-called branching ratio ( $BR = A_4/A_5$ ). The theoretical values for BR on the assumption of  $U^{3+}$  and  $Np^{3+}$  is 6 and 4, respectively. The experimental corrected values are: for USB 3.5(3) and for NpAs, 3.0(3). BR can be used to determine the ionic state of the actinide ion.



**Fig. R.38.** UX (X = N, P, As). Thermoelectric power,  $S$ , vs. temperature,  $T$ , for UN up to 1200  $^{\circ}\text{C}$  and UP and UAs up to 900 and 800  $^{\circ}\text{C}$ , respectively [64WP]. Note similar high values of  $S$  at RT, approaching 60  $\mu\text{V/K}$ , for all three mononictides, showing p-type conductivity.

**Fig. R.39.** For caption see next page

**Fig. R.39.** UX (X = C, N, P). **(A)** **(a)** Thermal conductivities,  $\kappa$  and **(b)** electrical resistivities,  $\rho$ , measured up to 1000 K on sintered samples [76KTM1]. **(B)** Three models are adopted in order to separate the thermal conductivity into electronic  $\kappa_{\text{el}}$  and phonon  $\kappa_{\text{ph}}$  components using the following formulae: 1)  $\kappa = \eta_0(L_0T/\rho) + \eta_1/T - \eta_2/T^2$ , 2)  $\kappa = \eta_0(L_0T/\rho) [1 - \exp(-T/\Delta + 0.2138)] + \eta_1/T - \eta_2/T^2$ , 3)  $\kappa = L_0T/\rho + \eta_1/T - \eta_2/T^2 [\log(1 + \eta_3T)]$ . The parameters  $\eta_0$ ,  $\eta_1$ ,  $\eta_2$  and  $\Delta$  were determined to get the best fit to the  $\kappa(T)$  curve (for further details see the original paper).  $L_0$  is the Sommerfeld value of 24.5 nW $\Omega$ /K<sup>2</sup>.

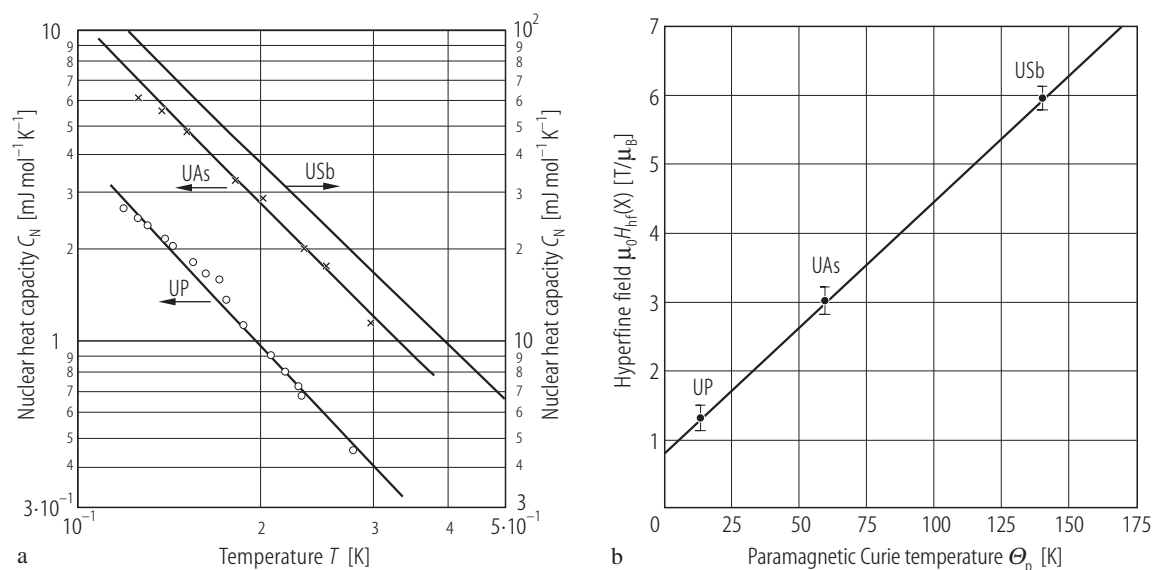


**Fig. R.40.** UX (X = P, As, Sb) s.c. **(a)** A log-log plot of nuclear heat capacity,  $C_N$ , vs. temperature,  $T$  [84RO], [85ROV2]. The solid lines show the  $T^{-2}$  behaviour. There is the one order of magnitude larger  $C_N$  of USb (see also Fig.V.70) with respect to  $C_N$  of UP and UAs. Hence  $C_N$  becomes a negligible contribution to  $C_p$  in the case of the latter monopnictides at temperatures above 1.5 K. **(b)** The

anion hyperfine fields  $H_{\text{hf}}(X)$  derived from a nuclear Schottky anomaly vs. the paramagnetic Curie temperature  $\Theta_p$  [84RO], [85ROV2].  $H_{\text{hf}}(X)$  for UP and USb were taken from [82RMV] and [76LMSV], respectively. For  $H_{\text{hf}}(\text{U})$  in UP and USb see [80BMHS]. The presented dependence indicates that  $H_{\text{hf}}(X)$  is directly related to the strength of interaction between the magnetic atoms.

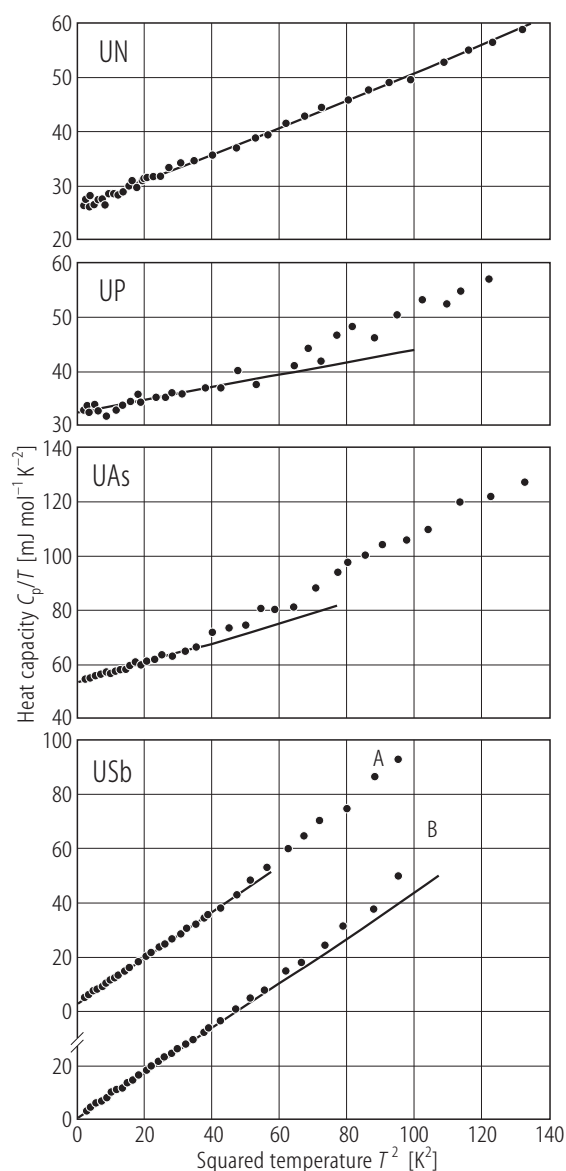


**Fig. R.41.** UX (X = N...Sb) s.c. The  $C_p/T$  vs.  $T^2$  plots for the uranium mononictides taken between 1.5...12 K. For USb the data for two different single crystals A and B are given [85ROV2]. The latter data differ from that given earlier (see [83RFOV]). For corresponding values of  $\gamma(0)$  see Table 3.

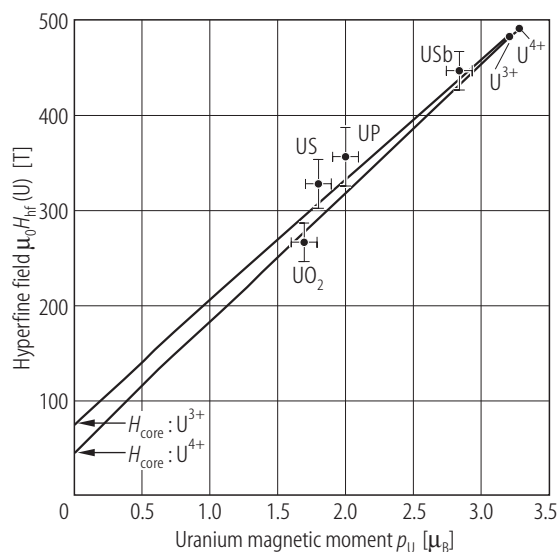


**Fig. R.42.** UX (X = P, Sb). Uranium hyperfine fields,  $H_{hf}(U)$ , vs. uranium magnetic moments,  $p_U$ , [72SKDK].  $H_{hf}$  arises from the orbital contribution and the polarization of the core electrons,  $H_{hf} = H_{orb} + H_{core}$ . The straight lines are drawn under assumptions of constant values (indicated) for  $H_{core}$  and of the proportionality  $H_{orb}$  to the magnetic moment  $p_0$ . The values  $H_{hf}$  of  $U^{4+}$  and  $U^{3+}$  as well as for US and  $UO_2$  are also plotted.

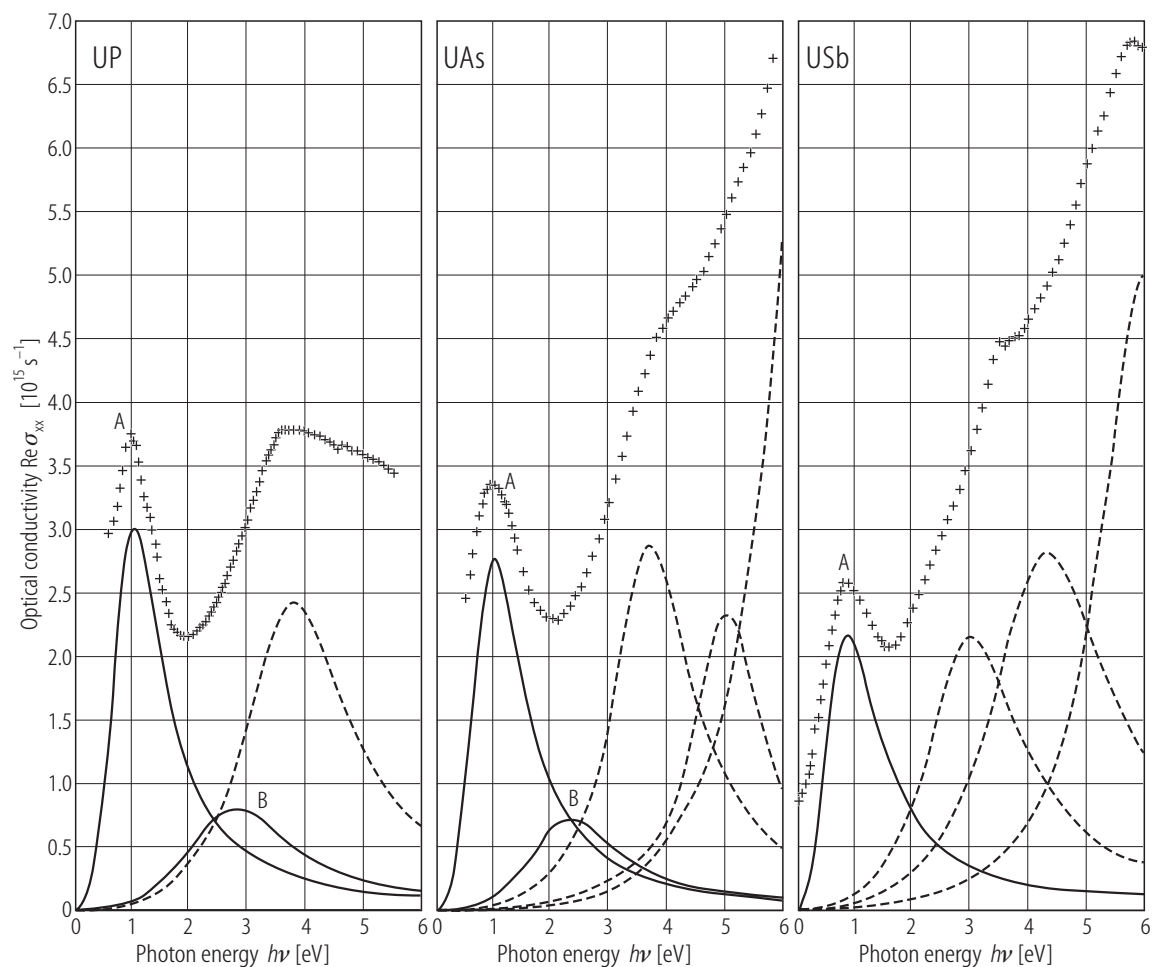
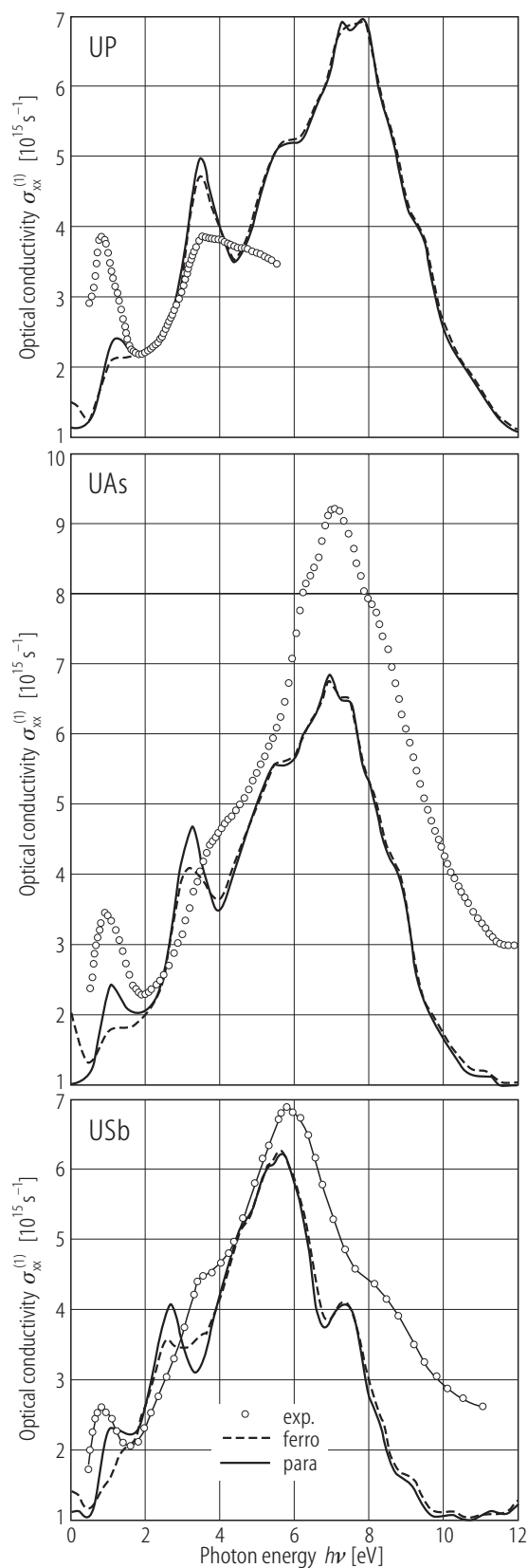


**Fig. R.43.** UX (X = P, As, Sb) s.c. The low energy part of the absorptive part of the diagonal conductivity  $\text{Re } \sigma_{xx}$  as a function of photon energy  $h\nu$  [98S]. This conductivity was obtained by a Kramers-Kronig transformation of NNIR measurements extending from 0.03 to 12 eV [80S2, 86SR] and decomposition into up to four Lorentzians and one

Drude term (see [86R]). The occurrence of two peaks A and B below the  $p \rightarrow d$  transition energy range are attributed to the  $f \rightarrow d$  and  $d \rightarrow f$  transitions, respectively. The lower energy of the former transition with respect to the latter is in contradiction with a molecular orbital calculation of [79SVK].



←

**Fig. R.44.** UX (X = P, As, Sb). Calculated *ab initio* optical conductivity,  $\sigma_{xx}^{(1)}$  vs. photon energy,  $h\nu$ , compared to available experimental data [05KO]. The calculations (lines) were performed assuming either a paramagnetic or a ferromagnetic state, using a constant lifetime broadening. The experimental data (symbols) for UP and UAs/USb are taken from [86R] and [80S3], respectively. The broad parts of spectra at 6...8 eV are caused by  $p \rightarrow d$  transitions, whereas the two peaks below 4 eV are due to  $f \rightarrow d$  and  $d \rightarrow f$  transitions.

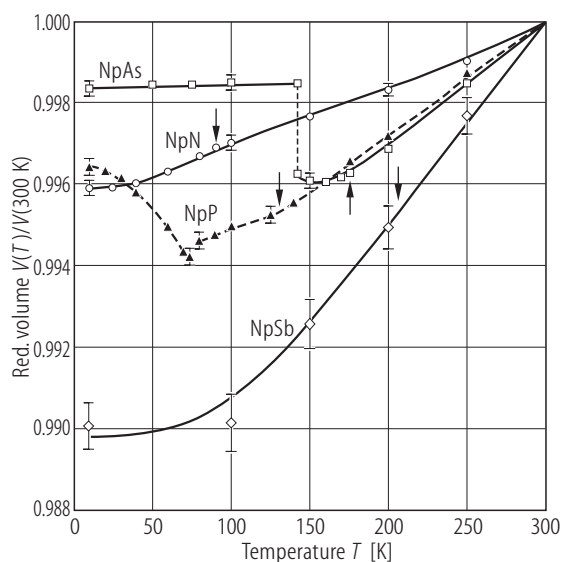


**Fig. R.45.** NpX (X = N,P,As,Sb). Reduced unit cell volume  $V(T)/V(300 \text{ K})$  as a function of temperature for neptunium monpnictides [74LM], [74ADHL] and [74MLKR]. Note that thermal expansion of the lattice is greater for the neptunium monpnictides with greater interatomic spacing. The arrows show the ordering temperatures for NpN ( $T_C = 87 \text{ K}$ ) and NpSb ( $T_N = 207 \text{ K}$ ) as well as for NpP ( $T_N = 130 \text{ K}$ ) and NpAs ( $T_N = 175 \text{ K}$ ). The volume contractions vary smoothly through the relevant transitions indicating that they are not of first order. For the two latter compounds which exhibit first order transitions into a complex magnetic structure at temperatures lower than  $T_N$ , discontinuity occurs in the volume. The figure was also presented in LB III/12c, p.433 (Fig.59).

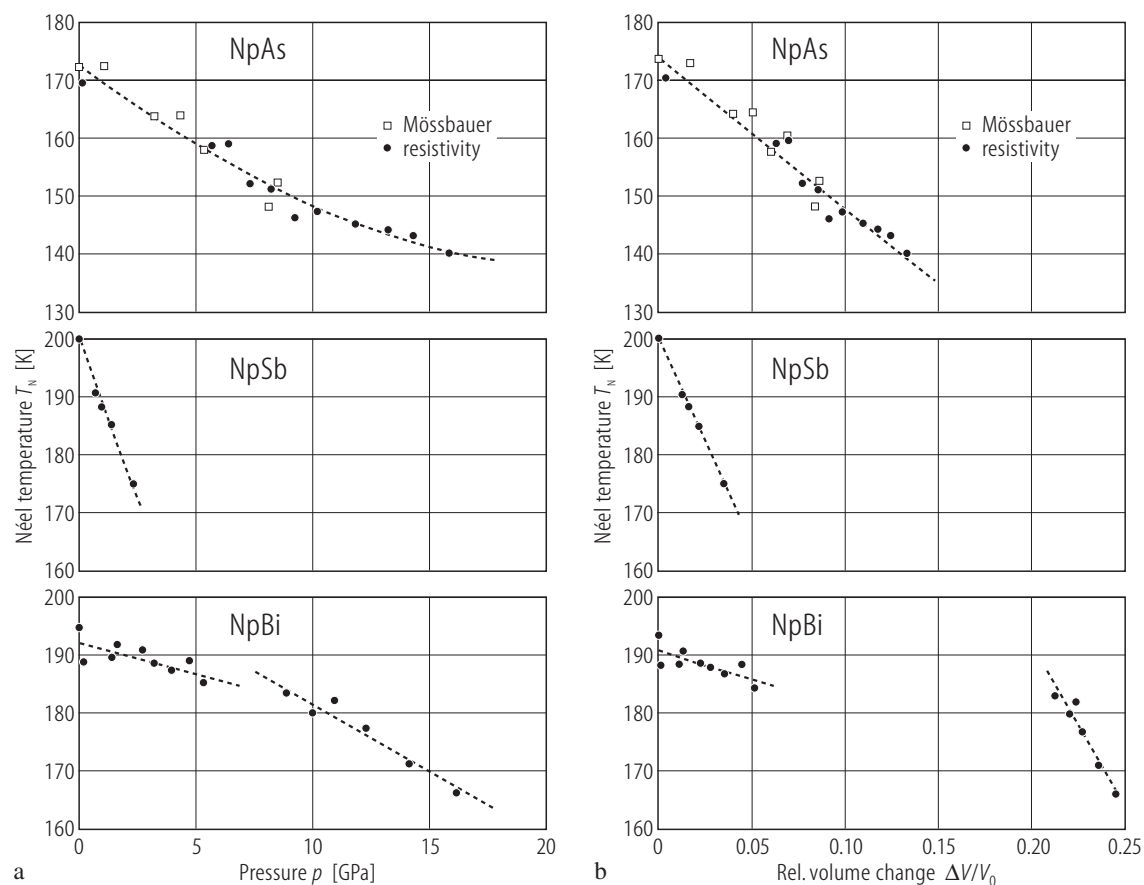


**Fig. R.46.** NpX (X = As, Sb, Bi). **(a)** Néel temperature,  $T_N$ , vs. pressure,  $p$ , determined in measurements of the resistivity (closed circles) and Mössbauer effect (open squares) [97IZBS]. Resistance data for NpAs and NpSb were taken from [94ABIB], while the Mössbauer data for NpAs from [89PMPZ]. **(b)** Néel temperature,  $T_N$ , vs.

relative volume change,  $\Delta V/V_0$ , determined from the resistance (closed circles) and Mössbauer data (open squares) [97IZBS]. The resistivity data for NpAs and NpSb are taken from [94ABIB], while the Mössbauer data for NpAs from [89PMPZ]

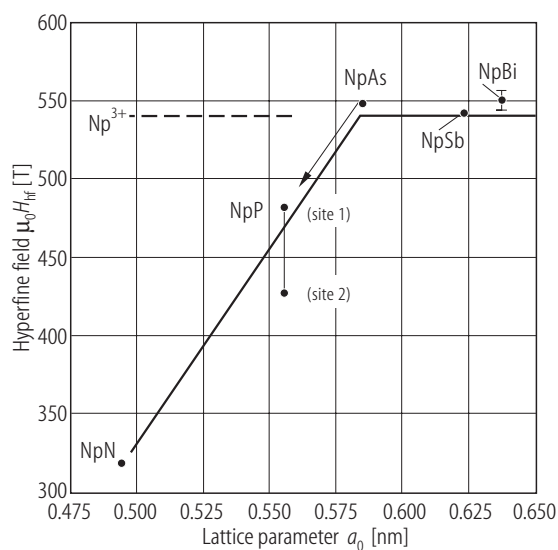


**Fig. R.47.** NpX (X = N...Bi). Hyperfine field,  $\mu_0 H_{hf}$ , of  $^{237}\text{Np}$  in the neptunium monopnictides vs. lattice parameters,  $a_0$ , [95K1]. The dashed line is  $B_{hf}$  for the free ion  $Np^{3+}$ .

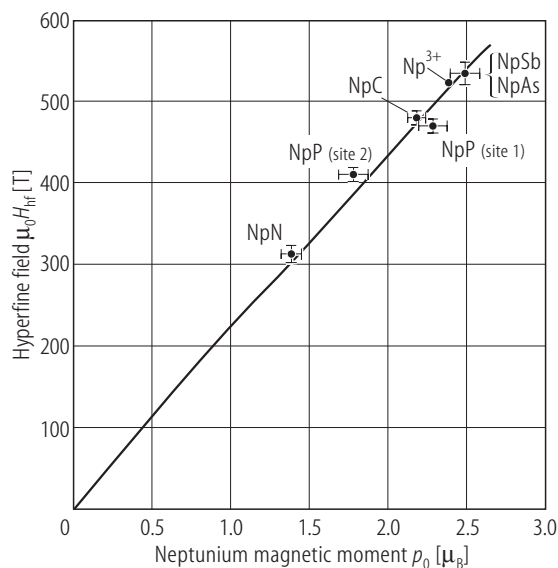


**Fig. R.48.** NpC, NpX (X = N...Sb). Relationship between hyperfine field  $H_{\text{hf}}$  and ordered magnetic moment  $p_0$  at 4.2 K for NpC [69DBKS], NpX (X = N, P, As, Sb) [73LDAN], [74ADHL] and free ion  $\text{Np}^{3+}(5f^4)$  without core polarization being included [72DK]. For all the series the linear relationship yielding a slope of  $215 \text{ T}/\mu_B$  shows that the electronic configuration of  $5f^4$  applies to all these compounds. See also [74DL] and [85DK]. An almost exact linear relation between the magnetic hyperfine field  $H_{\text{hf}}$  and the magnetic moments  $p_0$  has provided a very useful situation in Np-compound studies.

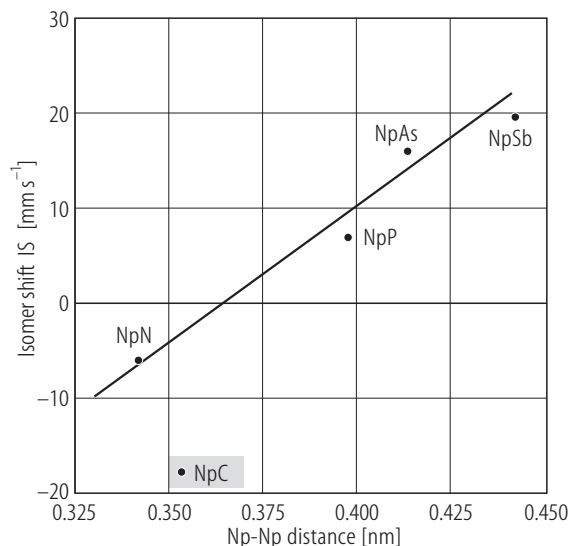
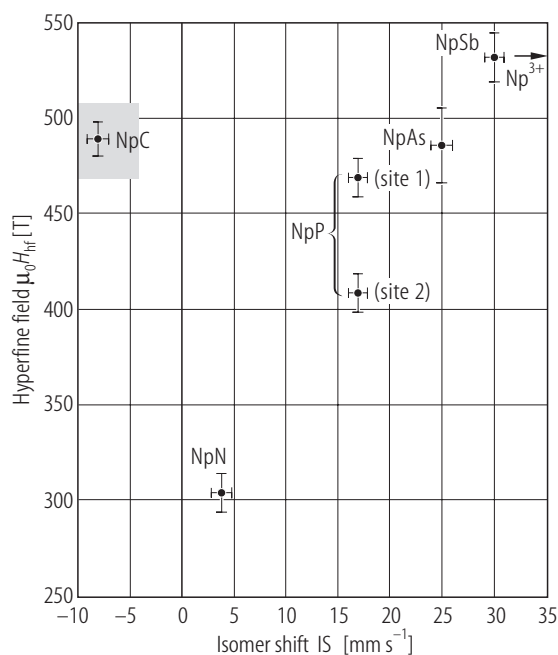


**Fig. R.49.** NpC, NpX. Isomer shift, IS, of  $^{237}\text{Np}$  vs. Np-Np distance based on [85DK]. Note that this dependence for NpC does not correlate with that (almost straight line) of the Np-mononictides.

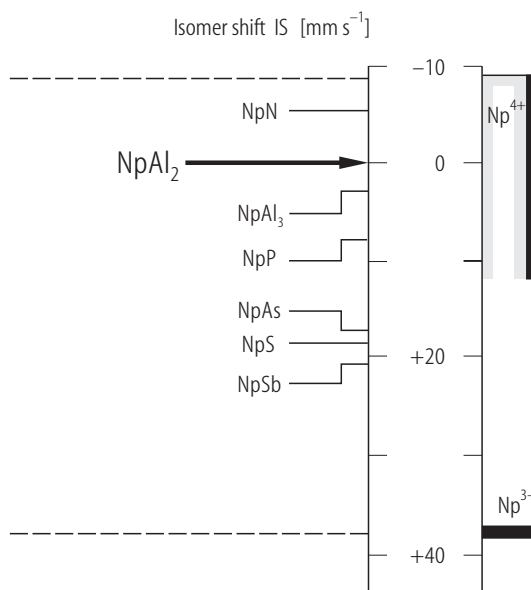


**Fig. R.51.** NpX (X = N, P, As, Sb and  $Y' = \text{S}'$ ). A fragment of the summary plot of isomer shift, IS, ( $\text{mm/s}$ ) with respect to  $\text{NpAl}_2$  and IS-ranges corresponding to the given Np-oxidation state [85DK].

←

**Fig. R.50.** NpC, NpX (X = N...Sb). Hyperfine field,  $H_{\text{hf}}$ , vs. isomer shift, IS, of  $^{237}\text{Np}$  in NpC and in the neptunium mononictides [85DK] and [88BBAK]. The  $H_{\text{hf}}$  free ion value of  $\text{Np}^{3+}$  is indicated by the arrow.



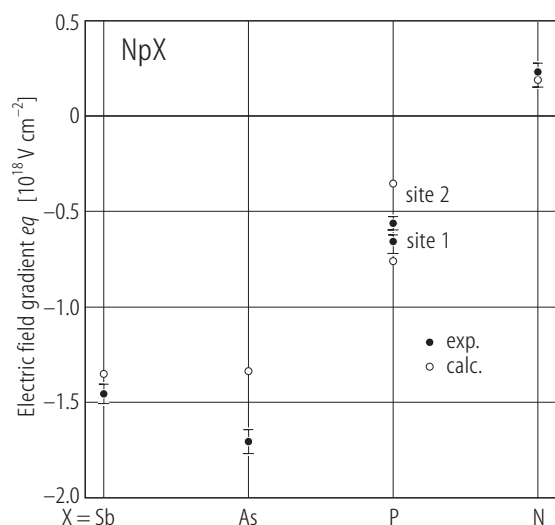


**Fig. R.52.** NpX (X = N, P, As, Sb). Measured and calculated values of electric-field gradient,  $eq$ , of  $^{237}\text{Np}$  in the neptunium monopnictides [85DK].

For Figs. R.53, R.54 see next pages

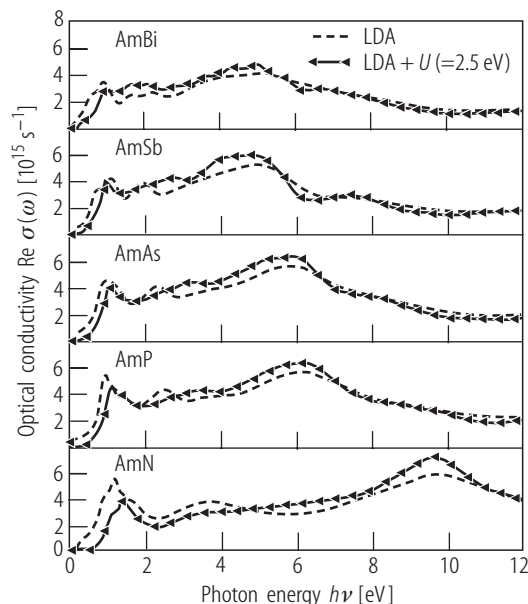


**Fig.R.56.** AmX (X=N...Bi). The absorptive part of the optical conductivity,  $\text{Re } \sigma(\omega)$ , computed by the LDA (dashed lines) and by LDA+ $U$  (solid lines) [05GDOB]. The conductivity spectra show for each monopnictide three major peaks. For AmN these are located just above 1 eV, 3.5 eV and around 9.5 eV. For the heavier anions these peaks shift successively to lower energies and e.g. for AmBi these peaks are located slightly below 1 eV, at 2 eV and about 5 eV. For the explanation of the location of each peak in view of the electronic transitions see the original paper.

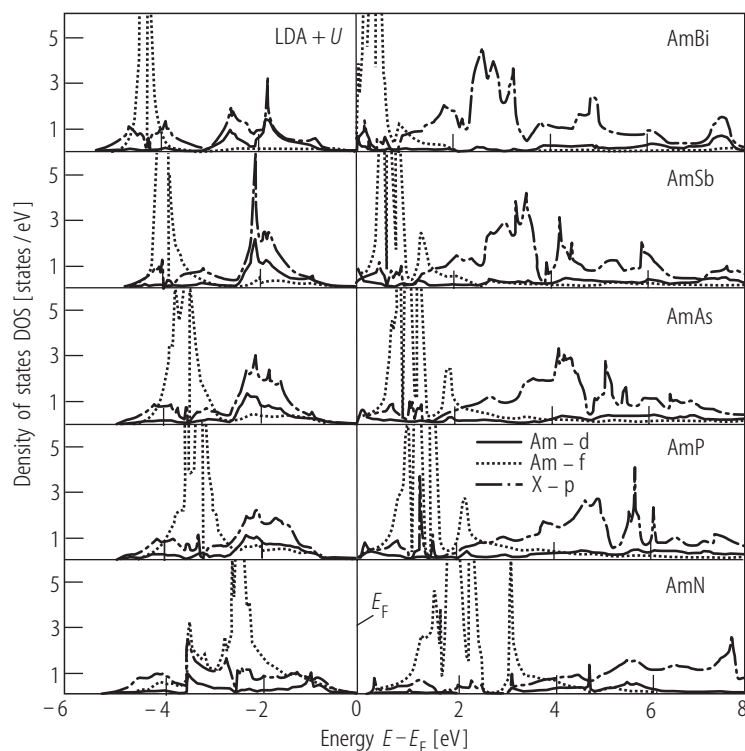


**Fig.R.55.** AmX (X=N...Bi). The LDA+ $U$  partial densities of states of the Am monopnictides ( $U=2.5$  eV). From these calculations a real semiconducting gap of 192 meV is predicted for AmN and a pseudogap in AmP to AmBi. The overlap between the f and d states of Am and p states of the pnictogen atom X results in the significant hybridization [05GDOB]. The calculated equilibrium lattice parameters for the AmX monopnictides by the LDA+ $U$  way give good agreement with available experimental data.

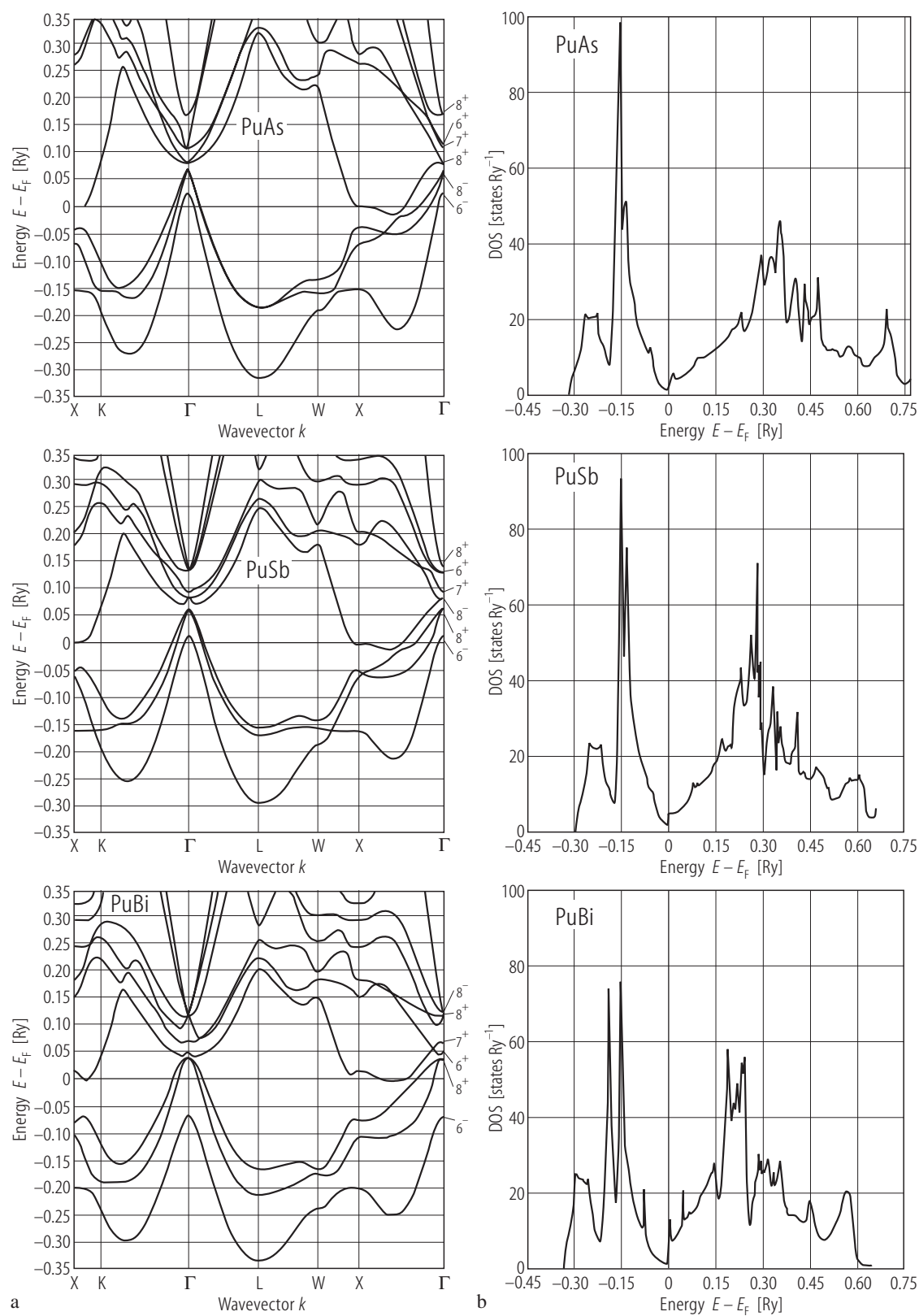


**Fig. R.53.** For caption see next page

**Fig. R.53.** PuX (X = As, Sb, Bi). **(a)** Band structure calculated along symmetry lines in the BZ by the LMTO method, where the Pu 5f states were treated as bound-core-like states [90WC]. The labels denote the symmetry of the bands at the  $\Gamma$  point:  $\Gamma_6^+$  (Pu 7s),  $\Gamma_6^-$  or  $\Gamma_8^-(X \text{ np})$  and  $\Gamma_7^+$  or  $\Gamma_8^+$  (Pu 6d). From first-principles a scheme for obtaining Anderson model Hamiltonian parameters for Pu mononictides is also presented [90WC]. **(b)** Density of states (DOS) corresponding to the relevant band structures [90WC].

**Fig. R.54.** PuX (X=As, Sb, Bi). The structural and elastic properties at high pressure of homolog pair (Ce-Pu) calculated by using an interatomic potential theory with modified ionic charge (solid and dashed lines) and compared to the experiment (closed points) [04SS]. **(A)** Equation of state of Pu mononictides. The experimental data are from [92BDHD], [89DBSP], and [99MHRR]. The good agreement between theory and experiment for the Pu mononictides indicates the mostly localized character of the 5f electrons which do not interact substantially with the lattice. **(B)** Phase transition pressures  $p_T$  for the Ce and Pu mononictides against principal quantum number of the 's' and 'p' subshells of the anion. Note that the B1→B2 transition pressures decreases systematically, consistently with the atomic number  $Z$  of the anion. Due to strong ionic bonding the plutonium mononictides (except for PuBi) need higher pressures to destabilize the B1-type structure than the Ce counterparts. **(C)** The calculated values of second order elastic constants  $c_{ij}$  and bulk modulus  $B_T$  for the Pu mononictides (values are given in the table below), compared with the Ce mononictides are plotted as a function of lattice parameters.

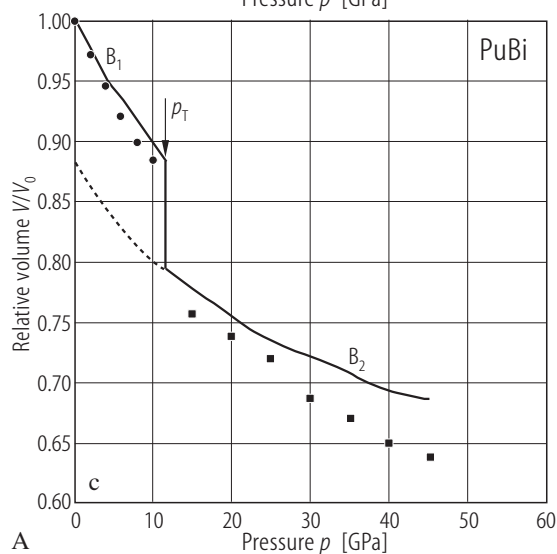
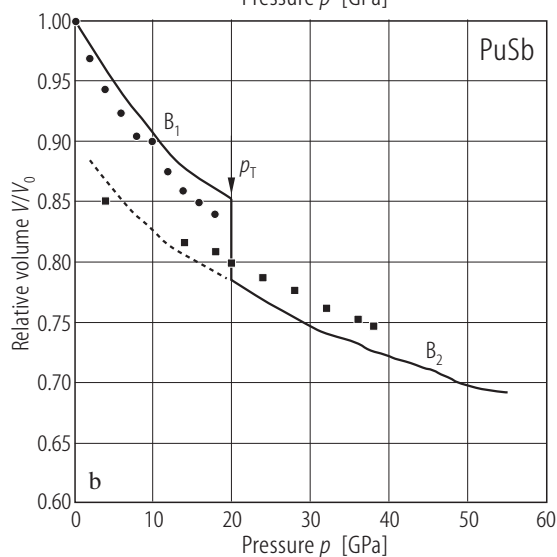
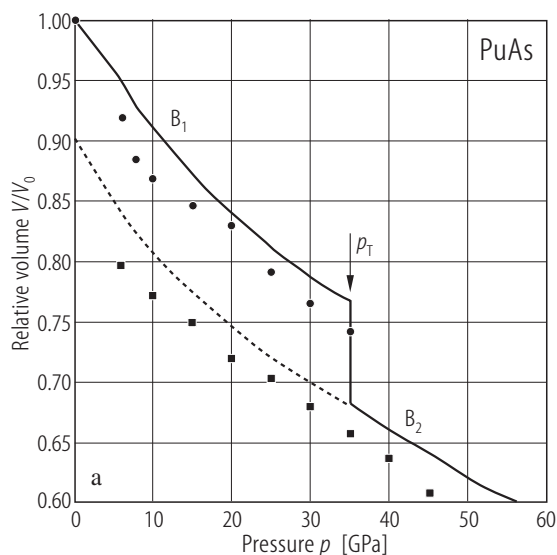
Table: Theoretical and experimental elastic constants and bulk moduli (in GPa)

Solids	$c_{11}$	$c_{12}$	$c_{44}$	$B_T$	
PuAs	152	25	25	67	
Experimental				69	[1]
PuSb	158	21	21	67	
Experimental				68	[1]
PuBi	147	20	20	62	
Experimental				61	[2]

[1] [87B], [95B]

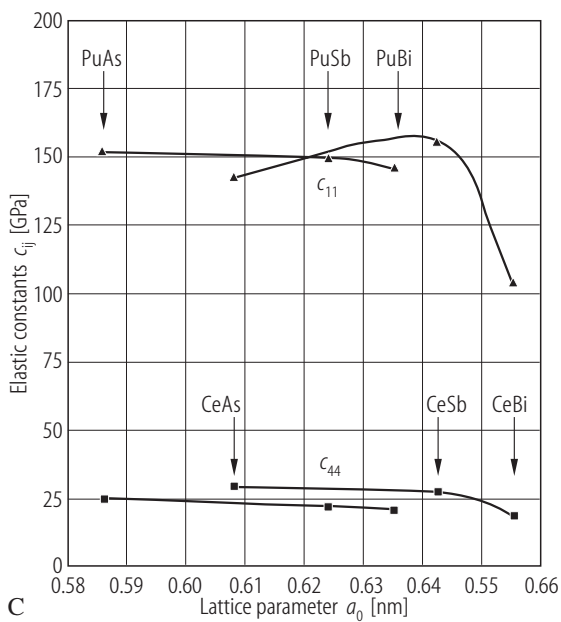
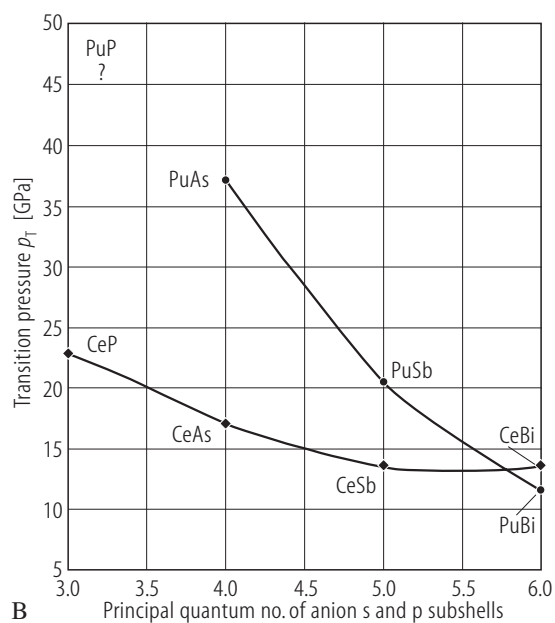
[2] [99MHRR]

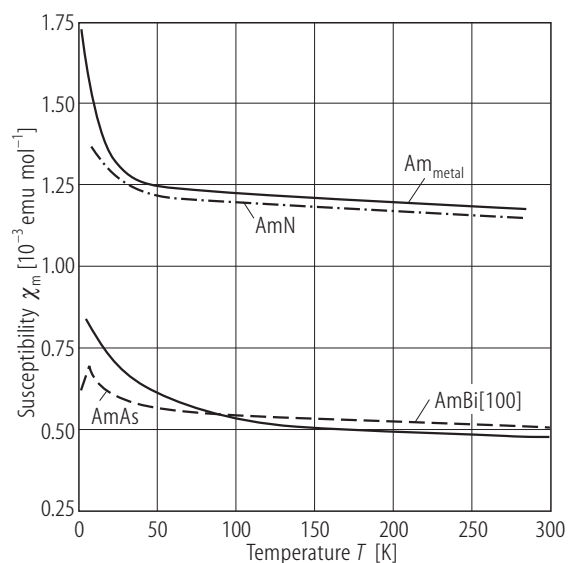
For Fig. R.54 see next page



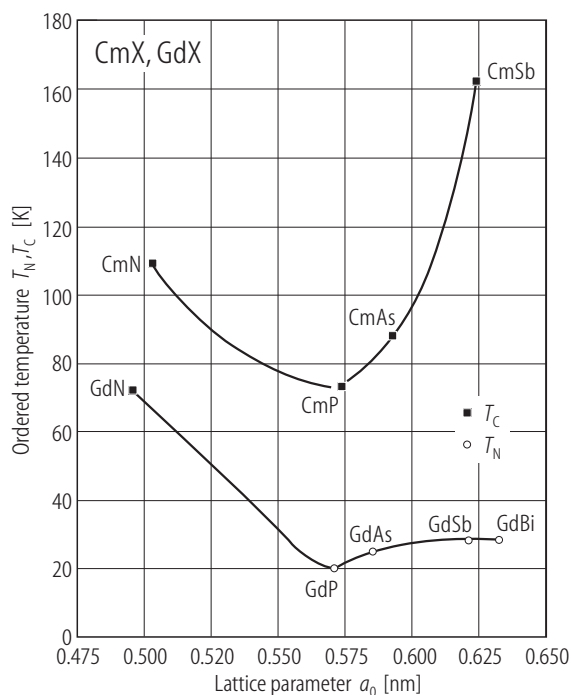
A

Fig. R.54. For caption see previous page





**Fig. R.57.** AmX (X = N, As, Bi). Molar magnetic susceptibilities of AmX, compared to that of Am metal, where the values for AmN and AmAs are taken from [76KCMM], while for AmBi and Am metal from [93VM]. In all cases the temperature-independent paramagnetism indicates the  $\text{Am}^{3+}$  ground state of  $J = 0$ . Note relatively high values of the susceptibilities, which have not found explanation so far.



**Fig. R.58.** CmX (X = N, P, As, Sb). Ordering temperatures, ( $T_N$ ,  $T_C$ ), vs. lattice parameter,  $a_0$ , for curium monopnictides as compared to those of isoelectronic gadolinium monopnictides [92MV]. Note a minimum in  $T_C$  for CmX at  $a_0 \approx 0.57$  nm. All the curium monopnictides are ferromagnets, the monopnictides of the lanthanide homologue of Cm, which is Gd (shown here for comparison), are antiferromagnets except for GdN, which is a ferromagnet.